This manuscript has been published online in: Dental Materials 2022 Nov

https://doi.org/10.1016/j.dental.2022.11.023

Toledano M, Osorio E, Aguilera FS, Osorio MT, Toledano R, López-López MT, Lynch CD, Osorio R.

Dexamethasone and zinc loaded polymeric nanoparticles reinforce and remineralize coronal dentin. A morpho-histological and dynamic-biomechanical study.

Dent Mater. 2023 Jan;39(1):41-56.

Title: Dexamethasone and zinc loaded polymeric nanoparticles reinforce and remineralize coronal dentin. A morpho-histological and dynamic-biomechanical study.

Authors: Manuel Toledano[a], Estrella Osorio[a], Fátima S. Aguilera[a*], María T. Osorio[a], Raquel Toledano[a], Modesto T. López-López[b], Christopher D Lynch[c], Raquel Osorio[a]

Institutions:

[a] University of Granada, Faculty of Dentistry. Colegio Máximo de Cartuja s/n 18071, Granada, Spain.

[b] University of Granada, Faculty of Science, Applied Physics Department. Av. Fuente Nueva s/ n 18071 Granada - Spain.

[c] University Dental School & Hospital/Cork University Dental School & Hospital, Cork, Ireland.

***Corresponding author:** Prof. Fátima S. Aguilera

University of Granada, Faculty of Dentistry

Dental Materials Section

Colegio Máximo de Cartuja s/n

18071 – Granada - Spain.

Tel.: +34-958249797

Fax: +34-958240809

Email: fatimas@ugr.es

Acknowledgements

This work was funded by Grant PID2020-114694RB-I00 funded by MCIN/AEI 10.13039/501100011033.

Declaration of interest: None.

Abstract

Objective. To investigate the effect of novel polymeric nanoparticles (NPs) doped with dexamethasone (Dex) on viscoelasticity, crystallinity and ultra-nanostructure of the formed hydroxyapatite after NPs dentin infiltration.

Methods. Undoped-NPs, Dex-doped NPs (Dex-NPs) and zinc-doped-Dex-NPs (Zn-Dex-NPs) were tested at dentin, after 24h and 21 d. A control group without NPs was included. Coronal dentin surfaces were studied by nano-dynamic mechanical analysis measurements, atomic force microscopy, X-ray diffraction and transmission electron microscopy. Mean and standard deviation were analyzed by ANOVA and Student-Newman-Keuls multiple comparisons ($p < 0.05$).

Results. At 21 d of storage time, both groups doped with Dex exhibited the highest complex, storage and loss moduli among groups. Zn-Dex-NPs and Dex-NPs promoted the highest and lowest tan delta values, respectively. Dex-NPs contributed to increase the fibril diameters of dentin collagen over time. Dentin surfaces treated with Zn-Dex-NPs attained the lowest nano-roughness values, provoked the highest crystallinity, and produced the longest and shortest crystallite and grain size. These new crystals organized with randomly oriented lattices. Dex-NPs induced the highest microstrain. Crystalline and amorphous matter was present in the mineral precipitates of all groups, but Zn and Dex loaded NPs helped to increase crystallinity.

Significance. Dentin treated with Zn-Dex-NPs improved crystallographic and atomic order, providing structural stability, high mechanical performance and tissue maturation. Amorphous content was also present, so high hydroxyapatite solubility, bioactivity and remineralizing activity due to the high ion-rich environment took place in the infiltrated dentin.

Dexamethasone and zinc loaded polymeric nanoparticles reinforce and remineralize coronal dentin. A morpho-histological and dynamic-biomechanical study.

Keywords: Apatite, Dentin, Dexamethasone, Polymeric nanoparticles, Remineralization, Transmission electron microscopy, Viscoelastic, X-ray diffraction, Zinc.

1. Introduction

Dentin, a part of the tooth which plays a critical role in responding to regeneration strategies and over all the mechanical strength of the tooth, represents a structure containing macro-micro and nano-characteristics. Dentin is a matrix of bundles of nanocrystalline hydroxyapatite (HAp), collagen fibers and web of dentin tubules [1]. This network span from the inner dental pulp to the interface between the dentin and enamel. It is radially distributed along the width of the dentin and possesses smaller tubules linking to adjacent tubules [2]. The composition of dentin is approximately 10% water, 20% organic structures and 70% inorganic structure [3].

In current dentistry, resin-based composite restorations pose the cutting edge due to the aesthetic appearance, the mechanical properties and their ability to bond to the dentin [4]. The adhesive bond layer integrity represents the most important factor that conditions the enduring success of restoratives [5]. Dentin demineralization and infiltration of resin are the first step to promote, clinically, resin-dentin bonding. During dentin demineralization, mineral ions are removed and the collagen matrix is exposed. Then, the demineralized collagen is resin infiltrated, and the hybrid layer is formed. At the bottom of the hybrid layer, a remaining fraction of demineralized and exposed collagen exists that is susceptible to degradation due to the presence of host-derived matrix metalloproteinases (MMPs) [6]. This leads to a reduction of the efficacy of bonding over time [7,8].

To achieve successive remineralization of dentin providing mineral precipitation within the hybrid layer, adhesives functionalization with bioactive materials have been used. Some nanoparticles (NPs) and fillers as hydroxyapatite (HAp), that perform as ceramic bioactive nanospheres [9], have been postulated to promote growing of minerals at the demineralized dentin. At a whole, they do not have an ideal degradation kinetics nor a well-regulated release [10,11]. Controlled delivery of drugs to reinforce the tissue is a determinant for the dentin treatment [12]. Currently, this can be achieved by increasing the use of NPs and the quick improvements of nanotechnology [13,14]. Polymeric NPs in addition to anionic carboxylate (*i.e.*, COO^-) groups located throughout the backbone of the polymer, may be doped with calcium (Ca-NPs), zinc (Zn-NPs), doxycycline (D-NPs) or melatonine (ML-NPs) to remineralize dentin [15]. However, it may be valuable to consider the indication of certain drugs with anti-inflammatory and possible remineralizing effects in some cases in which apical periodontitis exists.

The role of corticosteroids has attracted attention in the treatment of hard tissues. Dexamethasone (Dex) is a powerful synthetic glucocorticoid clinically used as an anti-inflammatory drug [16]. It has also been employed as a bioactive molecule for bone tissue [17], and to increase mineralization and expression of odontogenic markers in cultured stem cells from apical papilla [18]. As early as 1997, Hao et al [19] described the presence of significant growth in nodules containing needle-shaped crystals of HAp associated with a network of collagen fibrils, in a cultured medium containing Dex. Porous bio-sponges having high deacetylated chitosan and collagen type-1 doped with Dex have been fabricated to stimulate differentiation of stem cells and calcification of dentin [16]. Because of this, employing Dex through combination into biomaterials is promoted [17]. Corticoid has also been associated to an antibiotic (Lendermix) as intracanal medicament to strengthen dentin [20]. Basically, it was recommended as a common intracanal drug to

relieve acute apical periodontitis linked with postoperative pain or to prevent external imflammatory root resorption of the root in case of traumatically injured teeth [20]. The direct use of Dex is limited principally due to its toxic side effects and it has been proposed in the present research to use this corticoid loaded in polymeric NPs (Dex-NPs). Atomic force microscopy (AFM) nano-indentation is the most commonly used mean of testing the mechanical performance, including viscoelasticity, of materials or substrates [21], at nanoscale [22–25]. Hence, both morpho and nanomechanical properties can be obtained by using nanoscale dynamic mechanical analysis (nano-DMA), in a integrated way. During biting, as force bearing tissue, the strain distribution is an important indicator of the stiffness of teeth [26]. The complex organization of individual nanocrystals and their arrangement at higher size scales determines the mechanical performance of the resulting material, as the capacity to guide mineralization with spatial control is critical [27]. To study the hierarchical structure of biological minerals such as teeth and bone, X-ray diffraction (XRD) results as one of the most powerful techniques. TEM can provide high-resolution structural information along with crystallographic information when combined with Selected Area Electron Diffraction (SAED), with site-specific chemical analytic data when combined with Energy-Dispersive X-ray Spectroscopy (EDS), commonly used in scanning TEM (STEM), and with Fast Fourier Transform (FFT) when using High Resolution TEM (HRTEM).

Located in biological systems, zinc ions are considered MMPs' competitive inhibitors for the degradation of collagen, contributing to dentin matrix mineralization and organization [28]. Zinc participates in the increase of resin/dentin bonded interfaces' longevity [29]. Hence, an in depth in/ex vivo study involving remineralization processes in human teeth should be recommended to develop clinical approaches to obtain efficient dentin remineralization, first using Dex and then Dex plus Zn. Therefore, the purpose of this

study was to assess the efficacy of Dex-NPs and Zn-Dex-NPs to remineralize coronal dentin, throughout the assessment of its triboscopic properties, and both viscoelastic and crystallographic performance. The null hypothesis that was established is that Dex-NPs and Zn-Dex-NPs are not able to provoke differences in crystal morphology of dentin, triboscopic properties, dynamic mechanical performance and crystallinity.

2. Material and methods

2.1. Nanoparticles production and specimens' preparation

Active nanoparticles (NPs) of PolymP-n (NanoMyP, Granada, Spain) were obtained by polymerization precipitation. A thermodynamic approach has been employed to regulate the precipitation process: the Flory-Huggins model from Hansen's solubility parameters. The model was performed focusing on the polymer chains growth and the interactions of solvent molecules through hydrogen bonding, and dispersion and polar forces [30]. For the design of the NPs, 2-hydroxyethyl methacrylate worked as the backbone monomer, the functional monomer was methacrylic acid and the cross-linker was ethylene glycol dimethacrylate. NPs were then functionalized with Dex and Zn^{2+}. The NPs Dex loading process was performed *via* immersion of 10 mg of NPs in 5 mL of methanol and shaking during 3 minutes, which were weighed in two vials. Then, 0.75 mL of a solution of ZnCl2 (40 mg/l, phosphate buffer pH=7) were added to one of the vials, and 0.75 mL solution of Dex (40 mg/l, phosphate buffer pH=7) to the other one. Afterward, 30 mL of deionized water were added to both vials with NPs and experimental doping solutions, and NPs were incubated under shaking during 2 h. Then, they were centrifuged and dried in an oven at 45 ºC until constant weight. 2.5mg of Dex-NPs and 2.5mg of Zn-NPs were mixed and diluted in 0.5 mL of 96% ethanol to achieve a dispersion with both types of NPs in the same proportion, in order to form the Zn-Dex-NPs group. Three NPs-based groups

were developed, undoped-NPs, Dex-doped NPs (Dex-NPs) and Zn-doped-Dex-NPs (Zn-Dex-NPs).

Forty eight extracted unerupted human third molars stored in 0.5% chloramine solution at 4ºC for no longer than 1 month were randomly selected. The procedure followed the Declaration of Helsinki, and the protocol approval was undertaken by the Institution's Review Board (1906/CEIH/2020). All subjects signed the study informed consent. Teeth were sectioned horizontally to obtain dentin discs below the dentin/enamel junction, and these specimens were then polished to 180 grit SiC (silicon carbide abrasive paper) in order to generate a clinically relevant smear layer. The polished dentin areas were etched with phosphoric-acid for conditioning, washed and dried. Just an ethanol solution was applied (30 s) at the control group (untreated dentin) (i), or an ethanol suspension of undoped-NPs (ii), Dex-NPs (iii), Zn-Dex-NPs (iv) (NPs concentration was 1 mg/mL) for each of the four different study groups (n=12). After 30 s of ethanol evaporation, half of the specimens were stored in a dark environment in simulated body fluid solution (SBFS) for 24 h at 37 °C and the other half during 21 days.

2.2. Nano-DMA and Atomic Force Microscopy (AFM) analysis (nanoroughness and collagen fibril diameter)

Discs from each treated dentin were submitted for nano-DMA and AFM analysis. Nanomechanical properties were evaluated using a commercial nano-DMA package on a Hysitron Ti Premier nanoindenter (Hysitron, Inc., Minneapolis, MN). The nanoindenter tip was calibrated against a fused quartz sample using a quasistatic force setpoint of 2 µN to maintain contact between the tip and the sample surface (quasi-static signal frequency= 200 Hz). For the selected nano-DMA scanning parameters, the best-fit spherical radius approximation for the tip was 85 nm, based on a calibration-reduced modulus value of 69.6 GPa for fused quartz. A sinusoidal force of amplitude FA=0.10 µN and frequency

f=100 Hz was superimposed on the quasi-static force setpoint (Fq=2 μN), which was imposed for the samples modulus mapping. The dentin discs were then removed from the SBFS immersion and scanned under hydrated conditions. To eliminate problems associated to the meniscus forces transferred from fluid droplets to the indenter[31], and to preserve hydration of the dentin surfaces, a drop (1.5 mL) of 99.4% ethylene glycol [32] was applied on the polished surface of the specimen.

From the application of different models relating indentation force (F) and depth (D), the indentation modulus of the tested sample (E) under application of a quasi-static force (stable conditions) was obtained [33]. For each dentin disc, three modulus mappings were recorded. For each mapping and for each type of dentin surface, 15 value points of complex modulus (E^*), storage modulus (E'), loss modulus (E'') and tan delta (δ) were acquired. Areas of surfaces dentin around 10x10 μm were mapped to obtain data, with 0.2 Hz as frequency. For the topographical mapping, an atomic force microscope (AFM Nanoscope V, Digital Instruments, Veeco Metrology group, Santa Barbara, CA, USA) was employed on the same surfaces. At the extreme end of an oscillating cantilever, a 10 nm radius silicon nitride tip (Veeco) was mounted, intermittently contacting the surface at the lowest oscillation point. Vertical modifications of the AFM tip with a resonance frequency close to 330 kHz resulted in the height of the images shown as dark and bright zones. With a slow scan rate (0.1 Hz), digital images (10 x 10 μm) were captured for each dentin surface. To observe the dentin nanoroughness and fibril width of all groups (24 h and 21 d of storage), 5 random boxes of 1x1 μm were recorded for each image. The rest of the method was as in Toledano et al. (2018) [34]. Numerical data were further analyzed by ANOVA and Student-Newman-Keuls multiple comparison tests, with $p<0.05$ as statistical significance. The validity of the assumptions of normality and homoscedasticity of the data had been previously verified.

2.3. X-Ray Diffraction (XRD) and Transmission Electron Microscopy (TEM) analysis. Selected area diffraction and bright-field imaging

Dentin disc surfaces were then subjected to XRD analysis. In this work, an X-ray microdiffractometer (μXRD^2) was employed, which is a single crystal diffractometer. The system is equipped with a 2-dimensional detector system Cmos Photon 100 (Bruker-D8 Venture, Wien, Austria) and a 2D detector goniometer based on the XRD 2D scan software and kappa geometry. The X-ray beam (Cu Kα line, λ = 1.54 Å) was produced by a Cu microforms source Iμs and the generator settings were 50.00 kV/1.00 mA. The values of 2Θ scanning angles range were 10°-80°, with a distance specimen-detector of 40.00 mm. The exposure time for all measurements was 60 s and they were recorded at room temperature, 295 ± 0.1°K. The generator voltage used was 50.00 kV, with the Cu anode at a current of 1,000 mA. The rest of the method was as in Toledano et al. (2016) [35]. The procedure for the X-ray micro-diffraction pattern, the preferred orientation and the size of the crystallites were determined as indicated in Toledano-Osorio et al. (2021) [36]. Diffraction was acquired on an imaging plate, and from those digital plate data the intensity relationship was obtained using Origin Pro 2015. The diffraction peak positions were described to HAp in the JCPDS Card 9-432.

A Fei Titan 80-300 TEM-STEM microscope was used to analyze the specimens, operating at 300 kV, and equipped with a Cs CEOS image corrector and a high brightness electron gun (X-FEG) (ThermoFisher Scientific, Waltham, USA). The microscope is integrated with 4 energy dispersive X-ray analysis (EDX) detectors (FEI microanalysis Super X) as well as a high angle annular dark field detector (HAADF). Selected area electron diffraction (SAED) and bright-field (BF) patterns were also recorded. Scanning TEM (STEM) bright-field images were performed using the Super-X EDS system in the TEM [36]. To characterize each experimental group, selected mineral areas of interest

were displayed by the high-resolution transmission electron (HRTEM) imaging. A FEI Ceta camera was used for HRTEM images. The Fei Titan microscope was employed also to acquire two-dimensional compositional elemental mappings of the specimen using image drift correction and 300 kV of accelerating voltage. The map acquisition and two-dimensional compositional elemental analysis were completed within 5 min. STEM images from HAADF were acquired. All these images and the obtained maps were processed using the VELOX® software package [37]. In TEM imaging, Fast Fourier transforms (FFT) were computed from selected image areas.

3. Results

Attained viscoelastic moduli are displayed in Table 1. Figs. 1, S1, S2 and S3, contain scanning DMA analysis of dentin surfaces treated with the NPs included in the different groups of study. Figs. 2, S4 and S5 comprehend topographic images achieved by AFM of the interface formed in the different groups of study. Refined μXRD^2, Debye-Scherrer rings images and truncated μXRD^2 profiles are observed in Figs. 3, 4 and S6, respectively. TEM analysis of dentin surfaces treated with the different NPs may be seen in Figs. 5, 6, 7, S7, S8 and S9.

3.1. Nano-DMA analysis

The attained nano-DMA results of the samples were influenced by the storage time (P<0.05) and by the applied NPs type (P<0.05). Interactions among factors were significant (P<0.05). Table 1 and Figs. S1, S2 and S3 exhibit mean and SD of complex modulus (E*), loss modulus (E''), storage modulus (E') and tan (δ). At 24 h time point, undoped-NPs group attained the lowest complex modulus values, though both undoped-NPs and untreated dentin shared the highest E* values. After 24 h of storage, the property map of this interface at the peritubular areas achieved the highest resistance to dynamic

deformation, *E** (Fig. S1A). The 3-D contour map analysis of the storage modulus (*E'*) corresponds to this group (undoped-NPs) and unveils the highest elastic behaviors attained among groups (Fig. S1B). At 21 d of storage time, both groups doped with Dex exhibited the highest *E**, storage modulus (*E'*) and loss modulus (*E''*), among groups. In general, *E** increased in dentin samples treated with any kind of NPs, over time (Table 1). At 24 h time point, both groups doped with Dex exhibited the lowest *E'* indicating the lowest stiffness. *E'* increased in dentin treated with any Dex-doped NPs, over time (Table 1). At 24 h time point, dentin treated with undoped-NPs showed the lowest loss modulus (*E''*), among groups, showing the less amount of loss of energy. *E''* increased in dentin samples treated with undoped-NPs, meanwhile it remained similar in the rest of the groups (Fig. S2B). At 21 d of storage, the highest *E''* corresponded to samples treated with both Dex-NPs and Dex-Zn-NPs (Table 1). At 24 h time point, dentin samples treated with undoped-NPs attained the lowest tan delta (δ), and specimens treated with Dex-NPs showed the highest one, favoring the dissipation of energy through dentin structure. The 3-D contour map analysis (Fig. S2A) reflects the increase of tan delta (δ) in this group. At 21 d of storage time, dentin samples treated with Zn-Dex-NPs achieved the highest tan δ values. Tan δ values increased in dentin treated with undoped-NPs, decreased in samples treated with Dex-NPs and remained similar in samples treated with Dex-Zn-NPs, over time (Table 1). The property map of the interface promoted after Zn-Dex-NPs infiltration, at 21 d of storage, revealed areas of high values of *E** (Fig. S3C) and *E'* (Fig. 1B), identifying zones a high resistance to deformation and elastic behavior, respectively. Concerning *E'*, the locally measured moduli at intertubular dentin was represented in red, and the rest of the viscoelastic performance of the interface, in blue.

3.2. Atomic Force Microscopy (AFM) analysis

The nanoroughness (SRa) of dentin surfaces was influenced by the NPs type ($P< 0.05$) and by the time of storage ($P<0.05$). Interactions among factors were significant ($P<0.05$). Mean and SD of nanoroughness are presented in Table 2. At 24 h of storage, dentin surfaces treated with Zn-Dex-NPs attained the lowest roughness values; generalized dentin mineralization and zones of stress concentration were evidenced (Fig. S4D) in the same specimens. Areas of demineralization (Fig. S5C) and open dentinal tubules (Fig. 2B) were confirmed in samples treated with undoped-NPs, at 21 d of storage. At this time point of storage, dentin treated with Dex-NPs showed the highest SRa values with some empty dentinal tubules (Fig. 2C). Strong remineralization and some bridging processes were observed after 21 d when Zn-Dex-NPs were employed (Fig. 2D). SRa increased over time, except when undoped-NPs were applied, which made decrease the nanoroughness values. The bandwidth of the collagen fibrils were also influenced by the storage time ($P< 0.05$) and by the applied NPs type ($P<0.05$); factors interactions were also significant ($P<0.05$). Table 2 offers mean and SD of the fibrils width. At 24 h and 21 d of storage, samples treated with undoped-NPs reached the greatest bandwidths (98.51 nm) among groups. Samples treated with both undoped-NPs or Dex-NPs increased the fibril diameters over time (Table 2) (Figs. S5A, S5B).

3.3. X-Ray Diffraction (XRD) analysis

μXRD^2 analysis profiles of dentin showed that the physical broadening full width half maximum (FWHM) of peaks at 002, parallel to the c-axes, (2Θ, 25.900º; centroid peak position Θhkl, 0/0/-2; I, 10977386) reflection, after noting data plotted by the reduced full width and extended height at half maximum of the phosphate band, was lower in dentin samples treated with Zn-Dex-NPs (0.0072) when compared with the rest of the studied groups, after 21 d of SBFS storage (Table 3). At 24 h of storage, dentin surfaces treated with Dex-NPs achieved the lowest FWHM (Table 3), *i.e*, the highest crystallinity. Peaks

at 310, perpendicular to the *c*-axis, (2θ, 40.127° centroid peak position θhkl, −3/1/0; I, 1380390), after 21 d, dentin treated with undoped-NPs presented the lowest FWHM (0.0221), denoting a crystalline status, close to dentin treated with Zn-Dex-NPs (0.0222) (Table 1). At dentin treated with Dex-NPs after 21 d of storage, the highest peak (112) exhibited the maximum FWHM (more amorphous) (Figs. 3, S6D). When Zn-Dex-NPs was applied, after detecting the reflection at 211 peak (Fig. 3) and the diffraction ring equivalent to 211 and 112 planes (Fig. 4D), it may be distinguished higher crystallinity values than those obtained in the other groups (Table 3) (Fig. 4).

Table 3A presents a qualitative approximation of the size of the coherently scattering domain (*i.e*, the crystallite size). The longest and shortest [τ002 (H)] crystallite size, after 21 d of storage corresponded to dentin treated with both Zn-Dex-NPs (20.71 nm) and Dex-NPs (16.73 nm), respectively. The widest and narrowest [τ310 (L)] crystallite size, after 21 d of storage, corresponded to dentin treated with undoped-NPs (6.94 nm) and untreated dentin (5.75 nm), respectively (Table 3). Dentin treated with Zn-Dex-NPs showed the highest grain size at 002 plane (20.19 nm), and dentin treated with undoped-NPs at 310 plane (6.54 nm), after 21 d of storage (Table 3). The highest microstrain, after 21 d of storage appeared at dentin treated with Dex-NPs [τ002 (H)] ($1.92x10^{-6}$) and untreated dentin [τ310 (L)] ($1.7x10^{-5}$) (Table 3). Texture indices (R*hkl*) in dentin poly-crystalline structures were calculated. At 002 plane, the texture assessed with all NPs solutions followed the trend: undoped-NPs < untreated dentin < Zn-Dex-NPs < Dex-NPs. At 310 plane, the trend was: Dex-NPs < undoped-NPs < Zn-Dex-NPs < untreated dentin (Table 3).

3.4. Transmission Electron Microscopy (TEM) analysis (selected area diffraction and bright-field imaging), fast Fourier transform (FFT) spectroscopy and EDS analysis

Representative examples of HRTEM are included (Figs. 5, 6, 7 and S7). At 24 h, samples treated with Dex-NPs showed mainly starry polygonal block-like apatite crystals (Figs. S7A, S7B). The observed crystal size of the crystals conglomerate reported in the Fig. S7A was approximately 2 x 1 μm. The electron diffraction analysis showed the typical crystalline structure of crystals (Fig. S7C). Ca and P were detected as part of the elemental analysis by Energy dispersive X-ray (EDX) (Fig. S7D). STEM bright-field (Fig. S7E) and EDS-STEM two-dimensional elemental mapping at high magnification for calcium, phosphate and calcium phosphate (Figs. S7F, S7G, S7H, respectively) in dentin treated with Dex-NPs after 24 h of storage are shown. Ca density exceeded P density. Interplanar distances (Fig. S7C) were obtained, *d*, of 0.340 nm with a trajectory in two faced semicircles revealing the diffraction plane {002}. Interplanar distances, d, of 0.277 nm corresponded to the {112} for HAp. Both trajectories showed relative weak intensities, denoting amorphization.

At 24 h of storage and HRTEM analysis, specimens treated with Zn-Dex-NPs exhibited structures organized in three-dimensional agglomerated crystals (Fig. 5A) of polycrystalline nature (inset Fig. 6SA), when coronal dentin was analyzed. The observed crystal sizes commonly ranged from 100−200 nm. Polyhedral and starry needle-like apatite crystals were detected, after 21 d of storage when the control group was analyzed (Fig. 5B). The electron diffraction analysis exposed the typical both crystalline and amorphous structure of crystals (Inset Fig. 5B). Polymorphic needle-like apatite crystallites with multiple domains were observed when undoped-NPs were applied on dentin and observed after 21 d of storage (Figs. 5C, 5D). Crystalline matter was shown in the insets (inset Figs. 5C, 5D). The observed crystal sizes commonly ranged from 100−200 nm, in all cases. Scanning TEM (STEM) bright-field (Fig. 6E) and EDS-STEM

mapping for calcium, phosphate and calcium phosphate (Figs. 6F, 6G, 6H, respectively) in dentin treated with Zn-Dex-NPs after 21 d of storage are shown.

Interplanar distances (insets, Fig. 5), *d*, of 0.340-350 nm (high intensity) and 0.274-0.283 nm (low intensity), were obtained. For HAp, the diffraction plane corresponding to *d* = 0.340-350 nm with a margin of error of <1.50% was {002}. To *d* = 0.274-0.283 nm, the diffraction plane was {211}. For octocalcium phosphate (OCP), {121} a corresponding plane was set at interplanar distances of high intensity, and {511} the low intensity. β-tricalcium phosphate (β-TCP) showed {1010}as characteristic plane to a high intensity and no interplanar distance was assigned to the low intensity. Figs. 6A and 6B correspond with HRTEM analysis of a conglomerate of polymorph/polyhedral apatite crystals formed by plate-like overlapped polygons, crystalline in nature (Fig. 6C), from coronal dentin treated with Zn-Dex-NPs, at 21 d storage. This crystal showed a lower range of high crystallinity, as the interplanar distances only oscillated between 0.277 nm and 0.341 nm. The observed crystal sizes, within the conglomerate, generally ranged from 100−200 nm. Ca and P were detected as part of the elemental analysis by Energy dispersive X-ray (EDX) (Fig. 6D). STEM bright-field image was reproduced in Fig. 6E. Two-dimensional elemental mappings at high magnification of Ca (Fig. 6F), P (Fig. 6G) and PCa (Fig. 6H) were also observed in the area shown in Fig. 6E. Ca density exceeded P density, at a whole. The growth orientation and crystallite lattice of dentin samples treated with Zn-Dex-NPs, at 21 d storage are observed in the Fig. 7. The crystal lattice images are shown in Figs. 7A and 7C. The diffraction pattern [Fourier transform pattern (FTP) and inverse FTP] may be analyzed in Figs. 7B and 7D. Interplanar distances were also appreciated showing the highest intensity, with continuous trajectory, of the diffraction at *d* of 0.286 nm, confirming {211} as the diffraction plane. However, the d of 0.351 nm, with high intensity but with discontinuous trajectory, denoted {002} as the diffraction plane (Fig.

7B). Fig. 7D followed the same trend for intensities at *d* of 0.287 nm and 0.348 nm for diffraction planes of low and high intensities, respectively. These high relative intensities confirmed diffraction planes of HAp. The values of the relative intensities, expressed in percentages, for each group are expressed in Table S1.

4. Discussion

Dentin infiltration with Dex-NPs and Zn-Dex-NPs caused a favorable dissipation of energy through the crystalline remineralized dentin interface. Therefore, the null hypothesis must be rejected, as dentin application of Dex-NPs and Zn-Dex-NPs has significantly increased, over time, the complex, storage, loss moduli and made to vary tan δ of dentin treated with these loaded NPs (Table 1). In calcified tissues, improved mechanical properties are associated to intrafibrillar or functional remineralization [38,39]. Intrafibrillar mineralization is a pivotal factor to confirming that collagen fibrils show the same high mechanical performance as it happens in natural mineralized dentin [22].

The ratio that is established between the loss/the storage modulus (E''/E') can provide a general idea of the behavior of a viscoelastic material. Tan δ represents this quotient [40], indicating a measure of the relationship of the energy dissipated by the system to the energy stored in the system that allows its elastic recoil. It reveals how well a material can get rid of the energy. As observed, tan δ decreased [with a E' of ~236 GPa (Fig 1A) (Table 1)] when Dex-NPs were used, but increased when dentin was treated with Zn-Dex-NPs [with a E' of ~160 GPa (Fig 1B) (Table 1)], after 21 d of storage. As a result, a general tendency to lower amounts of accumulated energies at dentin surface can be observed over time, when dentin specimens were infiltrated with Zn-Dex-NPs. This high tan δ values complied with the decreased nanoroughness values (11.10 nm) that the dentin

treated with Zn-Dex-NPs showed when compared with those of dentin that treated with Dex-NPs (16.90 nm) (Table 2). Mineral maturation and intrafibrillar remineralization are commonly associated to a decrease in roughness [41]. This advance dentin maturity was morphologically accompanied of mineral deposition on the dentin surface.

AFM observations permitted to see totally filled tubules when using Zn-Dex-NPs at 21 d time point (Fig. 2D). Dentin mechanical properties are affected by occluded tubules [42,43]. Hence, strong mineral bundles within and around the tubules were observed in samples treated with Zn-Dex-NPs, at both 24 h (Fig. 4D) and 21 d (Fig. 2D) time points, where the majority of the entrances of dentin tubules were not observed. Peritubular dentin showed highly mineralized. When dentin was partially demineralized, some apatite remained in dentin, serving as nucleus on which calcium-phosphate crystals developed inside the tubules [11]. Similarly, NPs at the dentin surface are able to link to the collagen (Figs. S5A, S5B) favoring amorphous calcium-phosphate precursors precipitates, as ACP and β-TCP [44,45] accompanied by some other elements as magnesium, chloride and sodium (Fig. S9). From this anchor position, the polymeric NPs may facilitate a controlled ion release rate, or even NPs may function as carriers of other biological compounds, allowing tissue mineralization [46], that initiate in the dentin tubules at peritubular dentin (Yoshihara et al, 2020). The highest tan δ values attained (Table 1) by dentin samples treated with Zn-Dex-NPs, have become theoretically, associated to mineral precipitation at the intratubular space [42]. Surrounding the intratubular crystals, some bridges and rod-like new mineral formations were shown. These precipitated crystals attached the intratubular mineral deposits to the peritubular dentin (Fig. 2D).

Samples treated with Zn-Dex-NPs reflected the highest cristallinity (lowest FWHM) among groups in both 002 and 310 planes (Table 3), at 21 d of storage. Narrower peaks indicate less structural variation in bond angles and distances, as lower FWHMP denoted

an advanced crystallographic relative atomic order [47]. Crystallinity, low nanoroughness and improved tissue maturation have also been associated [41] (Table 2, Fig. 2D). Thus, samples treated with Dex-NPs and stored 21 d demonstrated lower crystallinity at both 002 and 310 planes (Table 3), performing an amorphization process [35] with higher degrees of impurities [36]. Incorporation of carbonate (CO_3^{2-}) facilitates immature hydroxyapatite and high biodegradability. The dissolution of hydroxyapatite creates an ion-rich environment with lower tan δ, high storage modulus *E′* and high loss modulus *E″* (Table 1) [48], and raises both supersaturation and the velocities of nucleation and growth of apatite nanocrystals [49]. The state of HAp as ultrafine nanocrystalline was also suggested from the resulted broadening [50]. A qualitative estimation of the size of the coherently scattering domain (*i.e.* the crystallite size) is reported in Table 3, where a decrease of the mean crystallite size alongside a direction parallel [002(*H*)] and perpendicular to the *c*-axis [310(*L*)] was obtained when Dex-NPs were applied on dentin and compared with the rest of NPs-treated samples. Crystallite size has been shown to increase with the maturation of the tissue [50], in calcified tissues, which is linked to crystallinity [51]. Therefore, this amorphization has become associated to the lowest crystallite size, low *H* and *L* values (16.31 nm and 6.75 nm, respectively) after 21 d storage time (Table 3). Besides, the patterns of diffractography gradually move from broad diffuse peaks at dentin infiltrated with Zn-Dex-NPs (24 h) to sharper and more crystalline peaks after 21 days (Fig. S6D), assuring that amorphous state is dynamic in nature [52]. On the other hand, AFM analysis permitted to observe specimens treated with Dex-NPs showing robust peritubular rings of mineral but with some entrance of tubules clearly discernible, at 21 d storage time (Fig. 2C). Remineralization was only partially and did not completely block the dentinal tubules. Within tubular structures, energy dissipation can happen *via* deformation in axial and radial trajectories [53], as confirmed

the AFM images. Microcracking (Fig. 2C) have been demonstrated in empty tubules. Otherwise, filled tubules can perform as uncracked-ligament bridging [54,55].

At a whole, considering the present outcomes, it is possible to (*i*) relate both contraction alongside the direction orthogonal to the *c*-axis and lower crystallinity in dentin infiltrated with Dex-NPs, and (*ii*) to partially take up that the higher thickness in crystallites, at dentin substrates infiltrated with Zn-Dex-NPs (20.71 and 6.92 nm at 002 and 310 planes, respectively) (Table 3), fits with a major maturity and mineralization in these samples. The assessment of μXRD^2 profiles also established high intensities of specimens infiltrated with Zn-Dex-NPs (Fig. S6D) at 211 and 112 peaks where diffractography patterns show HAp existence (red bars) with narrow and sharp crystalline peaks. Equally, the diffraction assessment described brighter rings after employing Zn-Dex-NPs than in the other samples (Fig. 4D), indicating higher line narrowing of peaks. At 21 d time point, in dentin samples infiltrated with Zn-Dex-NPs, in order to identify the crystal structure of mineral deposits SAED and EDS elemental mapping were obtained. EDS-STEM elemental mapping revealed a high P and Ca presence (Figs. 6F, 6G, respectively). Similarly, at Zn-Dex-NPs treated dentin, the diffraction XRD analysis formed brighter rings after 21 days (Fig. 6C) at 002, 211 and 112 planes (Fig. 4D, double arrows), in comparison with the 24 h time-point group (Fig. 5A), meaning low line broadening of peaks. In our observation, the P and Ca content indirectly reveals the formation of HAp [11] (Fig. 6H). In each calcium phosphate crystal, the relative intensity of the diffraction plane provided pivotal information for detecting the calcium phosphate phase when the orientation of the crystals were random [44]. After TEM analysis, the highest relative intensities of the {002} in the 0.341 nm (high intensity) [38% (Table S1)] and {211} in the 0.277 (low intensity) [100% (Table S1)] diffraction planes confirmed the greater presence of HAp in the mineral precipitates when Zn-Dex-NPs were used to infiltrate

dentin and analyzed at 21 d of storage, reflecting both Debye rings of HAp brighter intensities (Fig. 6C). The diffuse ring shown at SAED (Fig. S7C) when dentin was infiltrated with Dex-NPs pointed out a decline in crystallinity [56], likely amorphous calcium phosphate [57] (Figs. S7F, S7G, S7H) in junction other elements as silica, magnesium, chloride and sodium (Fig. S8). Amorphous calcium phosphate may be converted into HAp, at a later stage [11].

The presence of preferred grain orientation or texture is indicated by *R* values greater or lower than 1.0 [58,59]. Samples treated with both Dex-NPs and Zn-Dex-NPs schieved the closest values to this number, after 21 d of storage, (0.731 and 1.066, respectively), at 002 and 310 planes (Table 3), showing the most randomly orientation, in correspondence with strong chemical stability [60]. Therefore, distinct organization of nanocrystals depending on the type of applied NPs can be described, being mostly influenced by confined regions and angles defined by the surface topographies [25]. Hence, even at 24 h of storage time, crystals produced by Zn-Dex-NPs application exhibited less spaced nanocrystals, growing and settling compactly with much smaller co-alignment angles (Fig. 5A), than in case of Dex-NPs dentin treatment (Figs. S7A, S7B, S7E). The relative intensities at {002} (HAp) in the 0.340 nm (high intensity) [38% (Table S1)] and at {211} in the 0.274 (low intensity) [100% (Table S1)] appears somewhat weakened (Fig. 5A, inset), where three Debye rings, ranging from high (0.340 nm) to low (0.192 nm) intensity from the center, were identified. We speculate that both OCP and β-TCP may be more present than crystalline HAp, at the expenses of the relative high intensities of {121} and {1010}, respectively [44].

At 21 d storage in SBFS, TEM analysis of dentin infiltrated with Zn-Dex-NPs, revealed that minerals were composed of domains of locally oriented crystal arrays of submicron size crystals, which showed a well-defined lineation (Figs. 6A, 6B, 6E, 7A). Furthermore,

TEM analysis of a single nanocrystal and its fast Fourier transform (FFT) pattern revealed 15-25 nm length flat-ended nanocrystals with characteristic HAp morphology and composition of P and Ca (Figs. 6F, 6G, 6H) developing along the c-axis. These observations were further established by searching crystallographic orientation employing high-resolution TEM (HRTEM) (Fig. 7) and SAED (insets Fig. 5). It also means that the TEM data trend is consistent with our referenced texture values. Differences in growth orientation and co-alignment may be related with the preferential growth of the nanocrystals, involving significant effects on mechanical properties and morphology, at the macroscale, of the mineralized structures [25]. After 21 d, the faint preferred orientation (R_{hkl}) that was observed (Table 3) when dentin was treated with Zn-Dex-NPs (0.648) in comparison with samples treated with Dex-NPs (0.731) might indicate that these apatite crystallites created in the presence of zinc precipitated without any related biologically controlled mineralization procedure [61]. The principal ring pattern corresponding to 002 planes performing in the way of two semicircles instead of a continuous ring, when Zn-Dex-NPs were 21 days applied (Fig. 6C), illustrates that the crystallites have preferred orientation in c-direction [62]. As a consequence, dentin surfaces infiltrated with Zn-Dex-NPs have the trend towards random orientation, at 002 plane, over time, with negative nano-degradation [59] at 310 plane, as R_{hkl} decreased from 24 h (1.110) until 21 d (1.066) (Table 3). All these findings related with the local increase of ion concentration during mineralization of the collagen fibrils because the augmented localization of Ca and P ions within the collagen (Fig. 6D). The high intensities of the diffraction planes, mostly at the Debye ring that corresponds to the diffraction plane of low intensity {211} (0.277 nm, Fig. 6C) detected in dentin infiltrated with Zn-Dex-NPs confirmed the presence of crystalline HAp (Figs. 7B, 7D). Apart from that, H/L ratio increased in dentin treated with Zn-Dex-NPs more than in groups that used NPs (Table

3). This finding indicates a strong interaction of Zn-Dex-NPs with the HAp structure [63]. Partial dentin remineralization after undoped-NPs application was demostrated in the present study, as some demineralized collagen fibers and empty tubules, were shown at 21 d of storage (Fig. S5C). The decline of the mechanical properties in samples infiltrated with undoped-NPs in the control group, over time (Table 1), may be understood as a sight of dentin demineralization with further degradation [64] (Figs. 2A, 2B, S3C), meaning scarce remineralization potential at the intrafibrillar compartment. TEM pictures of untreated dentin (control) and dentin treated with undoped-NPs exhibited polyhedral/starry needle-like apatite crystals (Fig. 5B) of ~150 nm and polymorphic apatite crystals (Fig. 5C) of ~400-600 nm, respectively, leading to an amorphization process [65]. Samples treated with undoped-NPs (Fig. 5C) showed intermediate intensities at both Debye rings of HAp high {002} (0.350 nm) and low {211} (0.283 nm) intensities, probably due to a less relevant role of amorphous components, as OCP and β-TCP. Similar inset results may be interpreted in Fig. 5D, where the diffraction planes observed at high intensity {002} (0.340 nm) and low intensity {211} (0.275 nm) permit to infer the presence of amorphous components (Table S1).

These are, to the best of our knowledge, the only available results from Nano-DMA, AFM, μXRD^2, HRTEM/SAED, EDS-STEM and FFT combined methodologies aimed to analyze coronal dentin submitted to different doped-NPs treatment. After analyzing the data, numerically, some changes can be observed. The achieved differences are consistent with the distinct applied experimental processes, as it should be considered that assessments were obtained in biological *ex-vivo* samples. In previously works [66]. similar magnitude of differences have been published. Thereby, this investigation represents the first attempt to assess and interpret the viscoelastic performance and crystal ultrastructure of coronal dentin after applying dexamethasone-doped NPs. However, in

order to explore the action of nano-carried dexamethasone in dentin, in a more complete and profound way, several new techniques should be implemented. Dexamethasone liberation profile, sealing ability trough the fluid filtration system, Fourier-transform infrared spectroscopy (FTIR), Z potential, microtensile bond strength (MTBS), chemical characterization with Raman analysis, and field emission scanning electron microscopy (FESEM) would contribute to achieve this goal. The lack of these techniques into the present investigation may be considered a shortcoming of our methodology. From a clinical point of view, biocompatible and effective materials with biomimetic remineralization capability should be developed. A better understanding of the natural process of remineralizarion within the dentin interface is, therefore, essential, especially in case of using doped NPs.

5. Conclusions

Dentin treated with NPs enhanced its original mechanical properties over time, in general, though the presence of Dex in the NPs improved the mechanical performance when compared with the undoped-NPs. Dentin infiltration with both Dex-NPs and Zn-Dex-NPs remineralized the peritubular and intertubular areas, but the presence of Zn in the NPs promoted advanced intratubular precipitation of minerals. Samples treated with Zn-Dex-NPs attained higher maturity than those infiltrated with Dex-NPs and the greatest crystallinity among groups, being these crystals organized with randomly oriented lattices. Relative amorphization (poor crystallinity) was also observed in all samples, providing high hydroxyapatite solubility and remineralizing activity. Crystals produced by Zn-Dex-NPs application exhibited less spaced nanocrystals, growing and populating compactly with much smaller alignment angles. As a result, Zn-Dex-NPs might be considered as a feasible treatment for dentin reinforcement in endodontics, previous to

the canal filling, due to occlusion of dentinal tubules and the reinforcement of the dentin structure. All of this, after doing supplementary experimental tests to overcome the limitations of the present *in vitro* study.

Acknowledgements

This work was funded by Grant PID2020-114694RB-I00 funded by MCIN/AEI 10.13039/501100011033.

References

[1] Marshall GW, Marshall SJ, Kinney JH, Balooch M. The dentin substrate: structure and properties related to bonding. J Dent 1997;25:441–58. https://doi.org/10.1016/S0300-5712(96)00065-6.

[2] Xu S, Stranick M, Hines D, Du K, Pan L. Super high-quality SEM/FIB imaging of dentine structures without collagen fiber loss through a metal staining process. Sci Rep 2022;12:2369. https://doi.org/10.1038/s41598-022-06271-y.

[3] Tjäderhane L, Carrilho MR, Breschi L, Tay FR, Pashley DH. Dentin basic structure and composition—an overview. Endod Topics 2009;20:3–29. https://doi.org/10.1111/j.1601-1546.2012.00269.x.

[4] Muduroglu R, Ionescu AC, Del Fabbro M, Scolavino S, Brambilla E. Distribution of adhesive layer in class II composite resin restorations before/after interproximal matrix application. J Dent 2020;103:103494. https://doi.org/10.1016/j.jdent.2020.103494.

[5] Spencer P, Ye Q, Song L, Parthasarathy R, Boone K, Misra A, et al. Threats to adhesive/dentin interfacial integrity and next generation bio-enabled multifunctional adhesives. J Biomed Mater Res B Appl Biomater 2019;107:2673–83. https://doi.org/10.1002/jbm.b.34358.

[6] Hebling J, Pashley DH, Tjäderhane L, Tay FR. Chlorhexidine arrests subclinical degradation of dentin hybrid layers in vivo. J Dent Res 2005;84:741–6. https://doi.org/10.1177/154405910508400811.

[7] Carrilho MR, Tay FR, Donnelly AM, Agee KA, Tjäderhane L, Mazzoni A, et al. Host-derived loss of dentin matrix stiffness associated with solubilization of collagen. J Biomed Mater Res Part B Appl Biomater 2009;90:373–80. https://doi.org/10.1002/jbm.b.31295.

[8] Breschi L, Mazzoni A, Nato F, Carrilho M, Visintini E, Tjäderhane L, et al. Chlorhexidine stabilizes the adhesive interface: a 2-year in vitro study. Dent Mater 2010;26:320–5. https://doi.org/10.1016/j.dental.2009.11.153.

[9] Besinis A, van Noort R, Martin N. Remineralization potential of fully demineralized dentin infiltrated with silica and hydroxyapatite nanoparticles. Dent Mater 2014;30:249–62. https://doi.org/10.1016/j.dental.2013.11.014.

[10] Wu C, Zhang Y, Fan W, Ke X, Hu X, Zhou Y, et al. CaSiO3 microstructure modulating the in vitro and in vivo bioactivity of poly(lactide-co-glycolide) microspheres. J Biomed Mater Res Part A 2011;98A:122–31. https://doi.org/10.1002/jbm.a.33092.

[11] Yoshihara K, Nagaoka N, Nakamura A, Hara T, Hayakawa S, Yoshida Y, et al. Three-dimensional observation and analysis of remineralization in dentinal caries lesions. Sci Rep 2020;10:4387. https://doi.org/10.1038/s41598-020-61111-1.

[12] Yoo Y-J, Kwon I, Oh S-R, Perinpanayagam H, Lim S-M, Ahn K-B, et al. Antifungal effects of synthetic human Beta-defensin-3-c15 peptide on Candida Albicans–infected root dentin. J Endodont 2017;43:1857–61. https://doi.org/10.1016/j.joen.2017.06.035.

[13] Chieruzzi M, Pagano S, Moretti S, Pinna R, Milia E, Torre L, et al. Nanomaterials for tissue engineering In Dentistry. Nanomaterials-Basel 2016;6:134. https://doi.org/10.3390/nano6070134.

[14] Negi H, Saikia SK, Kanaujia R, Jaiswal S, Pandey R. 3β-Hydroxy-urs-12-en-28-oic acid confers protection against ZnONPs induced adversity in Caenorhabditis elegans. Environ Toxicol Phar 2017;53:105–10. https://doi.org/10.1016/j.etap.2017.05.004.

[15] Toledano M, Aguilera FS, Osorio E, Toledano-Osorio M, Escames G, Medina-Castillo AL, et al. Melatonin-doped polymeric nanoparticles reinforce and remineralize radicular dentin: Morpho-histological, chemical and biomechanical studies. Dent Mater 2021;37:1107–20. https://doi.org/10.1016/j.dental.2021.03.007.

[16] Alagha A, Nourallah A, Alhariri S. Dexamethasone- loaded polymeric porous sponge as a direct pulp capping agent. J Biomat Sci-Polym E 2020;31:1689–705. https://doi.org/10.1080/09205063.2020.1769801.

[17] Lim H-C, Nam OH, Kim M, El-Fiqi A, Yun H-M, Lee Y-M, et al. Delivery of dexamethasone from bioactive nanofiber matrices stimulates odontogenesis of human dental pulp cells through integrin/BMP/mTOR signaling pathways. Int J Nanomed 2016;11:2557–67. https://doi.org/10.2147/IJN.S97846.

[18] Shrestha S, Torneck CD, Kishen A. Dentin conditioning with bioactive molecule releasing nanoparticle system enhances adherence, viability, and differentiation of stem cells from apical papilla. J Endodont 2016;42:717–23. https://doi.org/10.1016/j.joen.2016.01.026.

[19] Jianjun H, Junnan S, Zhongying N, Wenxing X, Ling Y, Mingzhen X. Mineralized nodule formation by human dental papilla cells in culture. Eur J Oral Sci 1997;105:318–24. https://doi.org/10.1111/j.1600-0722.1997.tb00247.x.

[20] Nagas E, Cehreli ZC, Uyanik MO, Vallittu PK, Lassila LVJ. Effect of several intracanal medicaments on the push-out bond strength of ProRoot MTA and Biodentine. Int Endod J 2016;49:184–8. https://doi.org/10.1111/iej.12433.

[21] Poon B, Rittel D, Ravichandran G. An analysis of nanoindentation in linearly elastic solids. Int J Solids Struct 2008;45:6018–33. https://doi.org/10.1016/j.ijsolstr.2008.07.021.

[22] Balooch M, Habelitz S, Kinney JH, Marshall SJ, Marshall GW. Mechanical properties of mineralized collagen fibrils as influenced by demineralization. J Struct Biol 2008;162:404–10. https://doi.org/10.1016/j.jsb.2008.02.010.

[23] Bar-On B, Daniel Wagner H. Elastic modulus of hard tissues. J Biomech 2012;45:672–8. https://doi.org/10.1016/j.jbiomech.2011.12.003.

[24] Hu S, Li J, Liu L, Dai R, Sheng Z, Wu X, et al. Micro/nanostructures and mechanical properties of trabecular bone in ovariectomized rats. Int J Endocrinol 2015;2015:252503. https://doi.org/10.1155/2015/252503.

[25] Deng X, Hasan A, Elsharkawy S, Tejeda-Montes E, Tarakina NV, Greco G, et al. Topographically guided hierarchical mineralization. Materials Today Bio 2021;11:100119. https://doi.org/10.1016/j.mtbio.2021.100119.

[26] Fujisaki K, Todoh M, Niida A, Shibuya R, Kitami S, Tadano S. Orientation and deformation of mineral crystals in tooth surfaces. J Mech Behav Biomed Mater 2012;10:176–82. https://doi.org/10.1016/j.jmbbm.2012.02.025.

[27] Elsharkawy S, Mata A. Hierarchical Biomineralization: from nature's designs to synthetic materials for regenerative medicine and dentistry. Adv Healthc Mater 2018;7:1800178. https://doi.org/10.1002/adhm.201800178.

[28] Toledano M, Nieto-Aguilar R, Osorio R, Campos A, Osorio E, Tay FR, et al. Differential expression of matrix metalloproteinase-2 in human coronal and radicular sound and carious dentine. J Dent 2010;38:635–40. https://doi.org/10.1016/j.jdent.2010.05.001.

[29] Toledano M, Toledano-Osorio M, Hannig M, Carrasco-Carmona Á, Osorio MT, García-Godoy F, et al. Zn-containing adhesives facilitate collagen protection and remineralization at the resin-dentin interface: a narrative review. Polymers-Basel 2022;14:642. https://doi.org/10.3390/polym14030642.

[30] Medina-Castillo AL. Thermodynamic principles of precipitation polymerization and role of fractal nanostructures in the particle size control. Macromolecules 2020;53:5687–700. https://doi.org/10.1021/acs.macromol.0c00973.

[31] Ryou H, Amin N, Ross A, Eidelman N, Wang DH, Romberg E, et al. Contributions of microstructure and chemical composition to the mechanical properties of dentin. J Mater Sci Mater Med 2011;22:1127–35. https://doi.org/10.1007/s10856-011-4293-8.

[32] Pashley DH, Tay FR, Carvalho RM, Rueggeberg FA, Agee KA, Carrilho M, et al. From dry bonding to water-wet bonding to ethanol-wet bonding. A review of the interactions between dentin matrix and solvated resins using a macromodel of the hybrid layer. Am J Dent 2007;20:7–20.

[33] Han L, Grodzinsky AJ, Ortiz C. Nanomechanics of the cartilage extracellular matrix. Annu Rev Mater Res 2011;41:133–68. https://doi.org/10.1146/annurev-matsci-062910-100431.

[34] Toledano M, Toledano-Osorio M, Guerado E, Caso E, Osorio E, Osorio R. Assessing bone quality through mechanical properties in postmenopausal trabecular bone. Injury 2018;49 Suppl 2:S3–10. https://doi.org/10.1016/j.injury.2018.07.035.

[35] Toledano M, Aguilera FS, Osorio E, López-López MT, Cabello I, Toledano-Osorio M, et al. Submicron-to-nanoscale structure characterization and organization of crystals in dentin bioapatites. RSC Adv 2016;6:45265–78. https://doi.org/10.1039/C6RA02373H.

[36] Toledano-Osorio M, Aguilera FS, Muñoz-Soto E, Osorio E, Toledano M, Escames G, et al. Melatonin-doped polymeric nanoparticles induce high crystalline apatite formation in root dentin. Dent Mater 2021;37:1698–713. https://doi.org/10.1016/j.dental.2021.09.001.

[37] Martinez-Ruiz F, Paytan A, Gonzalez-Muñoz MT, Jroundi F, Abad MM, Lam PJ, et al. Barite formation in the ocean: Origin of amorphous and crystalline precipitates. Chem Geol 2019;511:441–51. https://doi.org/10.1016/j.chemgeo.2018.09.011.

[38] Toledano M, Vallecillo-Rivas M, Aguilera FS, Osorio MT, Osorio E, Osorio R. Polymeric zinc-doped nanoparticles for high performance in restorative dentistry. J Dent 2021;107:103616. https://doi.org/10.1016/j.jdent.2021.103616.

[39] Bertassoni LE, Stankoska K, Swain MV. Insights into the structure and composition of the peritubular dentin organic matrix and the lamina limitans. Micron 2012;43:229–36. https://doi.org/10.1016/j.micron.2011.08.003.

[40] Espino DM, Shepherd DET, Hukins DWL. Viscoelastic properties of bovine knee joint articular cartilage: dependency on thickness and loading frequency. BMC Musculoskelet Di 2014;15:205. https://doi.org/10.1186/1471-2474-15-205.

[41] Zurick KM, Qin C, Bernards MT. Mineralization induction effects of osteopontin, bone sialoprotein, and dentin phosphoprotein on a biomimetic collagen substrate. J Biomed Mater Res A 2013;101:1571–81. https://doi.org/10.1002/jbm.a.34462.

[42] Toledano-Osorio M, Osorio E, Aguilera FS, Medina-Castillo AL, Toledano M, Osorio R. Improved reactive nanoparticles to treat dentin hypersensitivity. Acta Biomater 2018;72:371–80. https://doi.org/10.1016/j.actbio.2018.03.033.

[43] Toledano-Osorio M, Aguilera FS, Osorio R, Muñoz-Soto E, Pérez-Álvarez MC, López-López MT, et al. Hydroxyapatite-based cements induce different apatite formation in radicular dentin. Dent Mater 2020;36:167–78. https://doi.org/10.1016/j.dental.2019.11.023.

[44] Karakida T, Onuma K, Saito MM, Yamamoto R, Chiba T, Chiba R, et al. Potential for drug repositioning of midazolam for dentin regeneration. Int J Mol Sci 2019;20:670. https://doi.org/10.3390/ijms20030670.

[45] Salaie RN, Besinis A, Le H, Tredwin C, Handy RD. The biocompatibility of silver and nanohydroxyapatite coatings on titanium dental implants with human primary osteoblast cells. Mater Sci Eng C Mater Biol Appl 2020;107:110210. https://doi.org/10.1016/j.msec.2019.110210.

[46] Toledano M, Osorio MT, Vallecillo-Rivas M, Toledano-Osorio M, Rodríguez-Archilla A, Toledano R, et al. Efficacy of local antibiotic therapy in the treatment of peri-implantitis: A systematic review and meta-analysis. J Dent 2021;113:103790. https://doi.org/10.1016/j.jdent.2021.103790.

[47] Schwartz AG, Pasteris JD, Genin GM, Daulton TL, Stavros Thomopoulos. Mineral distributions at the developing tendon enthesis. PLoS ONE 2012;7:e48630. https://doi.org/10.1371/journal.pone.0048630.

[48] Mestres G, Aguilera FS, Manzanares N, Sauro S, Osorio R, Toledano M, et al. Magnesium phosphate cements for endodontic applications with improved long-term sealing ability. Inter Endod J 2014;47:127–39. https://doi.org/10.1111/iej.12123.

[49] Chen C, Liu J, Sun F, Stansbury JW. Tuning surface microstructure and gradient property of polymer by photopolymerizable polysiloxane-modified nanogels. RSC Adv 2014;4:28928–36. https://doi.org/10.1039/C4RA02176B.

[50] Liu Y, Huang J, Li H. Synthesis of hydroxyapatite-reduced graphite oxide nanocomposites for biomedical applications: oriented nucleation and epitaxial growth of hydroxyapatite. J Mater Chem B 2013;1:1826–34. https://doi.org/10.1039/C3TB00531C.

[51] Olszta MJ, Cheng X, Jee SS, Kumar R, Kim Y-Y, Kaufman MJ, et al. Bone structure and formation: A new perspective. Mater Sci Eng R Rep 2007;58:77–116. https://doi.org/10.1016/j.mser.2007.05.001.

[52] Toledano M, Toledano-Osorio M, Medina-Castillo AL, López-López MT, Aguilera FS, Osorio R. Ion-modified nanoparticles induce different apatite formation in cervical dentine. Inter Endod J 2018;51:1019–29. https://doi.org/10.1111/iej.12918.

[53] Agrawal R, Nieto A, Chen H, Mora M, Agarwal A. Nanoscale damping characteristics of boron nitride nanotubes and carbon nanotubes reinforced polymer composites. ACS Appl Mater Interfaces 2013;5:12052–7. https://doi.org/10.1021/am4038678.

[54] Koester KJ, Ager JW, Ritchie RO. The effect of aging on crack-growth resistance and toughening mechanisms in human dentin. Biomaterials 2008;29:1318–28. https://doi.org/10.1016/j.biomaterials.2007.12.008.

[55] Shinno Y, Ishimoto T, Saito M, Uemura R, Arino M, Marumo K, et al. Comprehensive analyses of how tubule occlusion and advanced glycation end-products diminish strength of aged dentin. Sci Rep 2016;6:19849. https://doi.org/10.1038/srep19849.

[56] Wang F, Guo E, Song E, Zhao P, Liu J. Structure and properties of bone-like-nanohydroxyapatite/gelatin/polyvinyl alcohol composites. Adv Biosci Biotech 2010;1:185.

[57] Bodier-Houllé P, Steuer P, Voegel JC, Cuisinier FJ. First experimental evidence for human dentine crystal formation involving conversion of octacalcium phosphate to hydroxyapatite. Acta Crystallogr D Biol Crystallogr 1998;54:1377–81.

[58] Xue J, Zavgorodniy AV, Kennedy BJ, Swain MV, Li W. X-ray microdiffraction, TEM characterization and texture analysis of human dentin and enamel. J Microsc-Oxford 2013;251:144–53. https://doi.org/10.1111/jmi.12053.

[59] Low I-M. Depth-profiling of crystal structure, texture, and microhardness in a functionally graded tooth enamel. J Am Ceram Soc 2004;87:2125–31. https://doi.org/10.1111/j.1151-2916.2004.tb06369.x.

[60] Moshaverinia A, Ansari S, Moshaverinia M, Roohpour N, Darr JA, Rehman I. Effects of incorporation of hydroxyapatite and fluoroapatite nanobioceramics into conventional glass ionomer cements (GIC). Acta Biomater 2008;4:432–40. https://doi.org/10.1016/j.actbio.2007.07.011.

[61] Zavgorodniy AV, Rohanizadeh R, Swain MV. Ultrastructure of dentine carious lesions. Arch Oral Biol 2008;53:124–32. https://doi.org/10.1016/j.archoralbio.2007.08.007.

[62] Landau LD, Lifschitz, E.M. Statistical Physics (Part 1). vol. 5. 3rd ed. Oxford: Elsevier Ltd.; 1980.

[63] Bigi A, Boanini E, Gazzano M, Kojdecki MA, Rubini K. Microstructural investigation of hydroxyapatite-polyelectrolyte composites. J Mater Chem 2004;14:274–9. https://doi.org/10.1039/B308687A.

[64] Toledano M, Osorio R, Osorio E, Medina-Castillo AL, Toledano-Osorio M, Aguilera FS. Ions-modified nanoparticles affect functional remineralization and energy dissipation through the resin-dentin interface. J Mech Behav Biomed Mater 2017;68:62–79. https://doi.org/10.1016/j.jmbbm.2017.01.026.

[65] Lee SS, Huang BJ, Kaltz SR, Sur S, Newcomb CJ, Stock SR, et al. Bone regeneration with low dose BMP-2 amplified by biomimetic supramolecular nanofibers within collagen scaffolds. Biomaterials 2013;34:452–9. https://doi.org/10.1016/j.biomaterials.2012.10.005.

[66] Toledano-Osorio M, Aguilera FS, Muñoz-Soto E, Osorio E, Toledano M, Escames G, et al. Melatonin-doped polymeric nanoparticles induce high crystalline apatite

formation in root dentin. Dental Materials 2021;37:1698–713. https://doi.org/10.1016/j.dental.2021.09.001.

Figure and table captions

Fig. 1. A, Scanning mode nano-DMA analysis of the map of the storage modulus/*E'*, at the Dex-NPs/21 d group. In the color scheme shown, the redder color corresponds to higher values of the locally measured moduli. It became associated to the elastic energy released, at the peritubular dentin (arrows), after deformation. Asterisks and pointers represent *E'* of intertubular dentin and rest of the interface, respectively. **B**, 3-D contour map of the storage modulus (*E'*) distribution in a specimen at the Zn-Dex-NPs/21 d group. In the color scheme shown, the redder color corresponds to higher values of the locally measured moduli. Peritubular and intratubular dentin (arrows) showed the biggest elastic behavior (*E'*) as shown in the redder areas. Magnitudes of X and Y axis are in microns.

Fig. 2. AFM 15 x 15 μm top-view and surface plot image of untreated dentin (**A**) and dentin treated with undoped-NPs (**B**), at 21 d of storage. Open dentinal tubules (pointers) were observed. Both intertubular (ID) and peritubular dentin (PD) were discernible. **C**, AFM 15 x 15 μm top-view of topography mapping of dentin obtained after applying Dex-NPs at 21 d of storage time. Partially (pointers) or totally (asterisks) mineral filled tubules and "bridging"(arrows) processes are shown. **D**, AFM 15 x 15 μm top-view of topography mapping of dentin obtained after applying Zn-Dex-NPs and 21 d of storage. Both peritubular and intertubular dentin are evident. Intratubular dentin is totally occluding the dentinal tubules (asterisks). Faced arrows show Stick-slip images and double arrows point crack deflection and branching, around the peritubular cuff.

Fig. 3. Refined μXRD^2 profiles of control, undoped-NPs, Dex-NPs and Zn-Dex-NPs treated dentin after 21 d of SBFS storage. Vertical bars represent HAp (Hydroxyapatite) peaks. FWHM: Full Width at Half Maximum.

Fig. 4. Debye-Scherrer rings of untreated dentin (control) (**A**), dentin treated with undoped-NPs (**B**), Dex-NPs (**C**) and Zn-Dex-NPs (**D**) are shown. Double arrows, in D, mean strong diffraction rings.

Fig. 5. A, Bright-field of an assemblage of block-like apatite crystals ordered in three-dimensional agglomerated crystals (pointers) of coronal dentin treated with Zn-Dex-NPs at 24 h of storage, some of them organized in plate-like polygons (arrows). **B,** Bright-field of an assembly of a polyhedral and starry needle-like apatite crystals of coronal dentin used as control, and assessed at 21 d of storage. It is observed that the particles have a domain of locally aligned crystal arrays, showing the staggered order of polygon crystallites (scale bar: 200 nm). **C**, **D**, Bright-field of an assembly of polymorphic apatite crystals of coronal dentin treated with undoped-NPs-based compound, after 21 d storage. Magnified observation showing the in detailed strong needle-like apatite crystallites. The images reveal that the particles have multiple domains of locally aligned crystal arrays (scale bars: 100 nm).

Fig. 6. A, Bright-field of an assembly of polyhedral apatite crystals formed by plate-like overlapped crystals (pointers) of coronal dentin treated with Zn-Dex-NPs, at 21 d storage. **B**, Observation of the same section showing the in detailed polyhedral apatite appearance of crystallites on the right side. Aligned crystal arrays may be shown (arrows) (scale bars: 100 nm). **C**, A SAED of the crystal (+) shown in (B), at nanoscale. Two semicircles corresponding to 002 plane may be observed (arrowheads). **D**, Representative Energy-dispersive X-ray spectroscopy (EDX) of the crystals (+) observed in (B) showing the nanometer-sized apatite composition of calcium and phosphate as part of the elemental analysis. **E,** Scanning TEM (STEM) bright-field image and EDS-STEM mapping of the crystals (+) observed in (B). **F,** Two dimensional elemental mappings of phosphate [P] and calcium [Ca], (**G**), and calcium phosphate [PCa] (**H**).

Fig. 7. A, **C,** High Resolution TEM (HRTEM) images of a single hydroxyapatite nanocrystal showing the growth orientation and crystallite lattice, from a dentin sample treated with Zn-Dex-NPs and assessed after 21 d of storage. **B**, **D**, corresponding Fast Fourier Transform (FFT) diffraction pattern of hydroxyapatite nanocrystals from A and C, respectively.

Table 1. Mean and standard deviation (SD) of complex modulus (*E**) (GPa), storage modulus (*E´*) (GPa) and loss modulus (*E´´*) (GPa), and tan (δ) attained for experimental dentin-treated surfaces.

Table 2. Mean and standard deviation (SD) of nanoroughness and fibrils width in untreated and undoped nanoparticles (undoped-NPs), dexamethasone (Dex-NPs) and dexamethasone and Zn doped nanoparticles (Zn-Dex-NPs) treated dentin.

Table 3. Micro-X-ray diffraction pattern analysis approach of the experimental groups.

Fig. 1

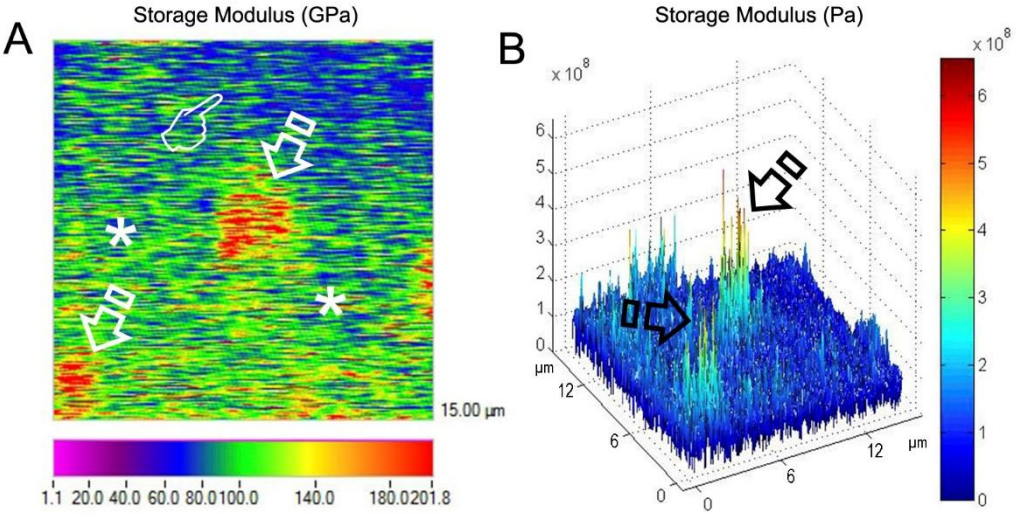
A
Storage Modulus (GPa)
15.00 µm
1.1 20.0 40.0 60.0 80.0 100.0 140.0 180.0 201.8
B
Storage Modulus (Pa)
x 10^8
µm
µm

Fig. 2

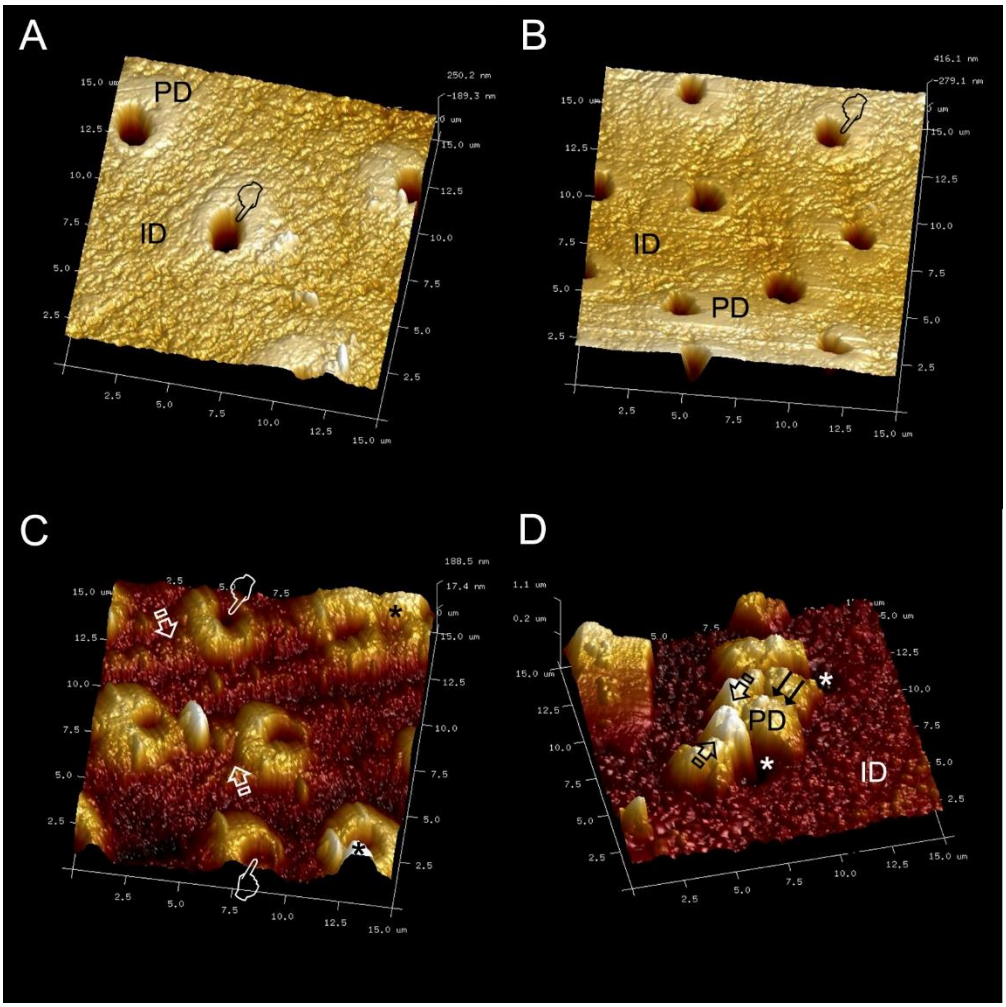
A
PD
ID
B
ID
PD
C
D
PD
ID

Fig. 3

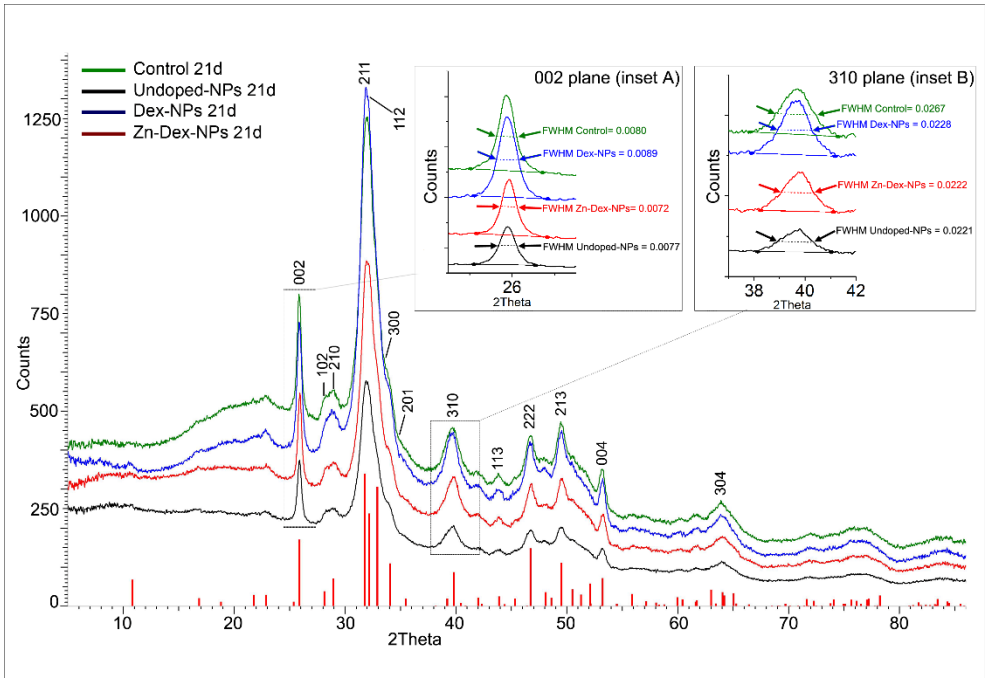
Control 21d
Undoped-NPs 21d
Dex-NPs 21d
Zn-Dex-NPs 21d
Counts
2Theta
002
102
210
211
112
300
201
310
113
222
213
004
304
002 plane (inset A)
FWHM Control= 0.0080
FWHM Dex-NPs = 0.0089
FWHM Zn-Dex-NPs= 0.0072
FWHM Undoped-NPs = 0.0077
310 plane (inset B)
FWHM Control= 0.0267
FWHM Dex-NPs = 0.0228
FWHM Zn-Dex-NPs = 0.0222
FWHM Undoped-NPs = 0.0221

Fig. 4

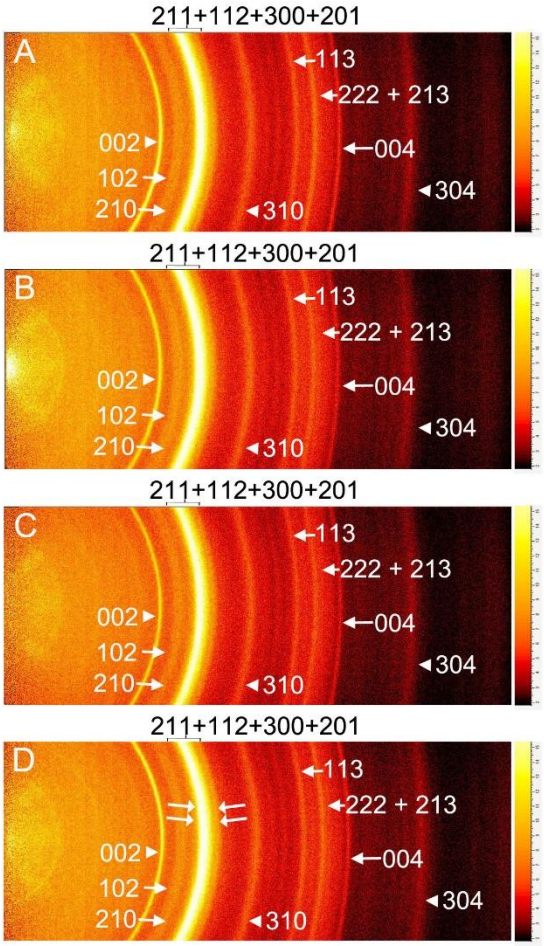
211+112+300+201
A
113
222 + 213
002
004
102
304
210
310
211+112+300+201
B
113
222 + 213
002
004
102
304
210
310
211+112+300+201
C
113
222 + 213
002
004
102
304
210
310
211+112+300+201
D
113
222 + 213
002
004
102
304
210
310

Fig. 5

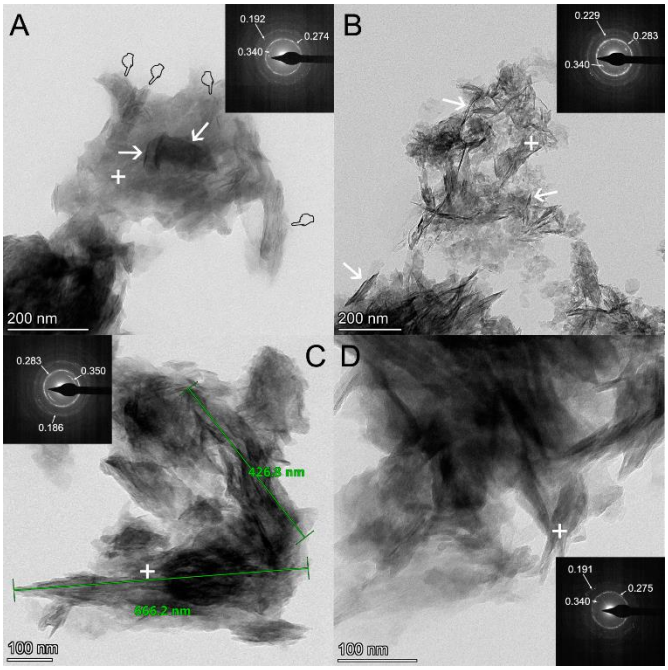
A
0.192
0.274
0.340
200 nm
B
0.229
0.283
0.340
200 nm
C
0.283
0.350
0.186
426.8 nm
866.2 nm
100 nm
D
0.191
0.275
0.340
100 nm

Fig. 6

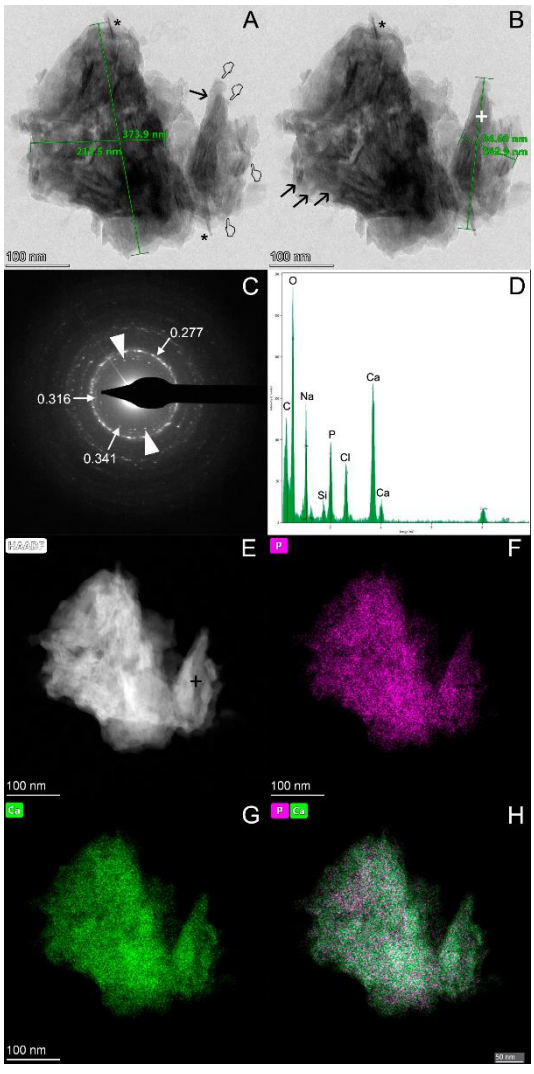
A
373.9 nm
212.5 nm
100 nm
B
100 nm
C
0.277
0.316
0.341
D
O
C
Na
P
Cl
Si
Ca
Ca
E
F
100 nm
Ca
G
P
Ca
100 nm
H
100 nm

Fig. 7

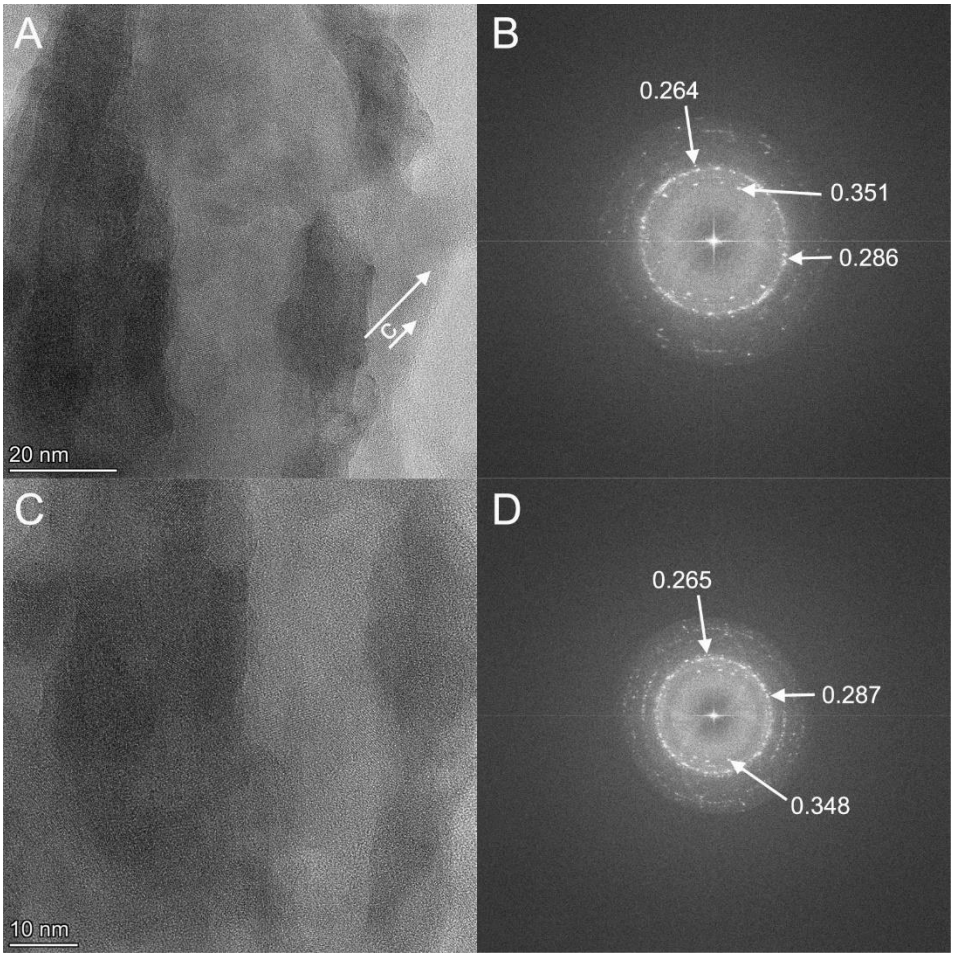

Table 1.

	Control		**Undoped-NPs**		**Dex-NPs**		**Zn-Dex-NPs**	
	24h	21d	24h	21d	24h	21d	24h	21d
CM(*E**) (GPa)	28.09 (6.51) a1	91.14 (26.43) A2	20.29 (32.51) ab1	113.92 (18.60) A2	8.86 (4.94) b1	234.82 (52.47) B2	19.10 (9.05) b1	156.37 (16.12) C2
SM(*E´*) (GPa)	27.85 (3.30) a1	92.02 (23.25) A2	90.67 (35.79) b1	113.72 (18.97) A1	4.53 (3.56) c1	236.03 (54.51) B2	14.86 (6.59) d1	160.83 (14.17) C1
LM(*E´´*) (GPa)	1.82 (1.23) a1	1.99 (0.70) A1	0.38 (0.10) b1	1.49 (0.73) A2	5.94 (3.10) a1	4.09 (1.33) B1	5.92 (1.88) a1	3.64 (1.07) B1
Tan(δ) Delta	0.20 (0.08) a1	0.04 (0.01) A2	0.01 (0.001) b1	0.04 (0.01) A2	1.47 (0.46) d1	0.03 (0.001) B2	0.51 (0.06) c1	0.49 (0.01) C1

Abbreviations: NPs: nanoparticles; Dex-NPs: dexamethasone doped NPs; Zn: zinc; Dex-Zn-NPs: dexamethasone and Zn doped NPs. CM: complex modulus; SM: storage modulus; LM: loss modulus; tan (δ): tan delta. Similar letters indicate no significant differences among treatment groups in the same storage period (lower case, 24h; upper cases, 21d). Similar numbers indicate no significant differences between the two storage periods (24h or 21 days) in the same treatment group.

Table 2.

	A. Nanoroughness		B. Fibrils width	
Group	**24 h** (SRa, nm)	**21 d** (SRa, nm)	**24h** (nm)	**21d** (nm)
Control	8.54 (1.61) a1	12.35 (1.90) a2	50.54 (6.23) A	56.68 (11.18) A
Undoped-NPs	66.47 (21.70) b1	12.62 (1.62) a2	98.51 (14.22) B*	139.29 (25.37) B
Dex-NPs	3.77 (0.67) c1	16.90 (2.63) b2	39.04 (5.56) C*	69.29 (6.23) A
Dex-Zn-NPs	2.29 (0.40) d1	11.10 (1.23) a2	173.14 (25.48) D*	55.35 (5.16) A

Abbreviations: Undoped NPs: Undoped nanoparticles; Dex-NPs: dexamethasone doped NPs; Zn: zinc; Dex-Zn-NPs: dexamethasone and Zn doped NPs. Same lower case indicates no statistical differences in nanoroughness between treated dentin groups. Same number indicates no statistical differences in nanoroughness between 24h and 7 days storage groups. Same capital letters indicate no statistical differences in fibrils width between treated dentin groups. * indicates no statistical differences in fibrils width between 24h and 7 days storage groups.

Table 3.

		002 plane					310 plane					
Group	**Storage time**	**FWHM**	***H*: Scherrer equation (nm) (τ)**	**Scherrer-Wilson equation (nm)**	**Microstrain %**	**R_{hkl}**	**FWHM**	***L*: Scherrer equation (nm) (τ)**	**Scherrer-Wilson equation (nm)**	**Microstrain %**	**R_{hkl}**	***H/L***
Control	24 hs	0.0080	18.49	18.02	$1.58x10^{-6}$	0.641	0.0241	6.39	6.02	$1.3x10^{-5}$	1.180	2.89
	21 d	0.0080	18.59	18.12	$1.56x10^{-6}$	0.638	0.0267	5.75	5.42	$1.7x10^{-5}$	1.156	3.23
Undoped-NPs	24 hs	0.0082	18.18	17.72	$1.63x10^{-6}$	0.678	0.0222	6.92	6.52	$1.2x10^{-5}$	1.170	2.63
	21 d	0.0077	19.32	18.83	$1.44x10^{-6}$	0.618	0.0221	6.94	6.54	$1.2x10^{-5}$	1.116	2.78
Dex-NPs	24 hs	0.0069	21.49	20.95	$1.17x10^{-6}$	0.652	0.0238	6.47	6.09	$1.3x10^{-5}$	0.942	3.32
	21 d	0.0089	16.73	16.31	$1.92x10^{-6}$	0.731	0.0228	6.75	6.36	$1.2x10^{-5}$	1.194	2.48
Zn-Dex-NPs	24 hs	0.0080	18.60	18.14	$1.56x10^{-6}$	0.645	0.0243	6.34	5.97	$1.4x10^{-5}$	1.110	2.93
	21 d	0.0072	20.71	20.19	$1.26x10^{-6}$	0.648	0.0222	6.92	6.52	$1.2x10^{-5}$	1.066	2.99

Abbreviations: FWHM. Full-width half-maximum; NPs: Nanoparticles; Dex: Dexamethasone.

Supporting Information

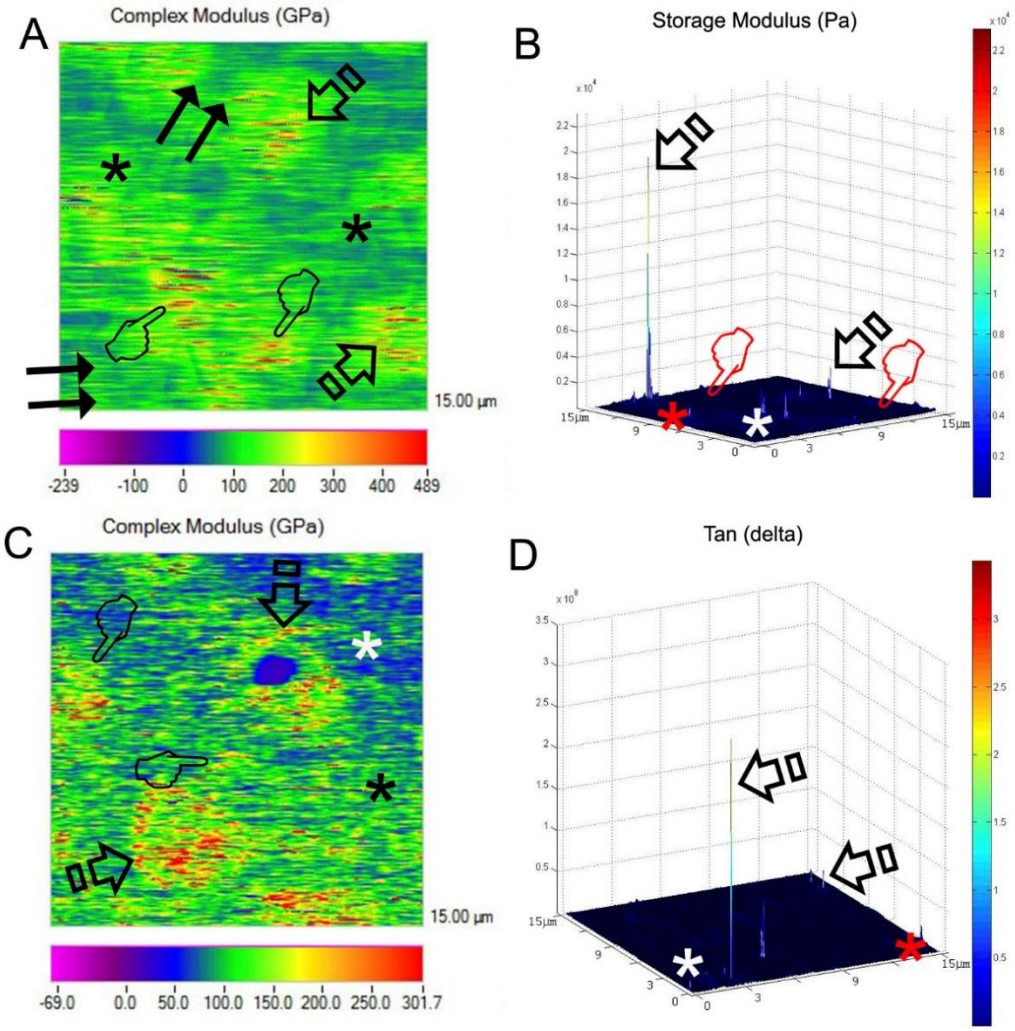

Fig. S1. **A**, Scanning mode nano-DMA analysis of the map of the complex modulus/*E** (A), at the undoped-NPs/24 h group. In the color scheme shown, the redder color corresponds to higher values of the locally measured moduli. Interconnected and non-regular yellow-greenish color point out areas of *E** associated with peritubular dentin (arrows). The maximum complex modulus became linked to the redder areas, potentially related to peritubular and intratubular mineralization (pointers). The intertubular dentin area was represented, at the mapping, by the greenish blue fringe (asterisks), and the demineralized dentin located at the bottom of the infiltrated dentin appeared in bluish green (double arrows). **B**, 3-D contour map of the storage modulus (*E'*) distribution in a specimen at the undoped-NPs/24 h group. In the color scheme shown, the redder color corresponds to higher values of the locally measured moduli. Peritubular dentin (arrows) showed the highest elastic behavior (*E'*) as shown in the redder areas, meanwhile both intertubular dentin (asterisks) and infiltrated dentin (pointers) achieved similar values of *E'*, as shown in the clearest blue zones. Magnitudes of X and Y axis are in microns. **C**, Scanning mode nano-DMA analysis of the map the complex modulus/*E**, at the undoped-NPs/21 d group. In the color scheme shown, the redder color corresponds to higher values of the locally measured moduli. Wider circles of higher complex modulus, represented in red are unveiled (arrows), corresponding to the peritubular dentin. They are immersed in an extended area of a lower *E**, represented at the mapping in yellow (pointers), corresponding with the intertubular dentin. The rest of the interface appears in blue and green (asterisks). **D**, 3-D contour map of the tan δ distribution in a specimen at the Dex-NPs/24 h group. In the color scheme shown, the redder color corresponds to higher values of the locally measured moduli. At the NPs-dentin inter-diffusion zone, tan δ attained high values (arrows) creating a zone of lower dissipation of energy at the interface, and thereby promoting stress concentration (asterisks). Magnitudes of X and Y axis are in microns.

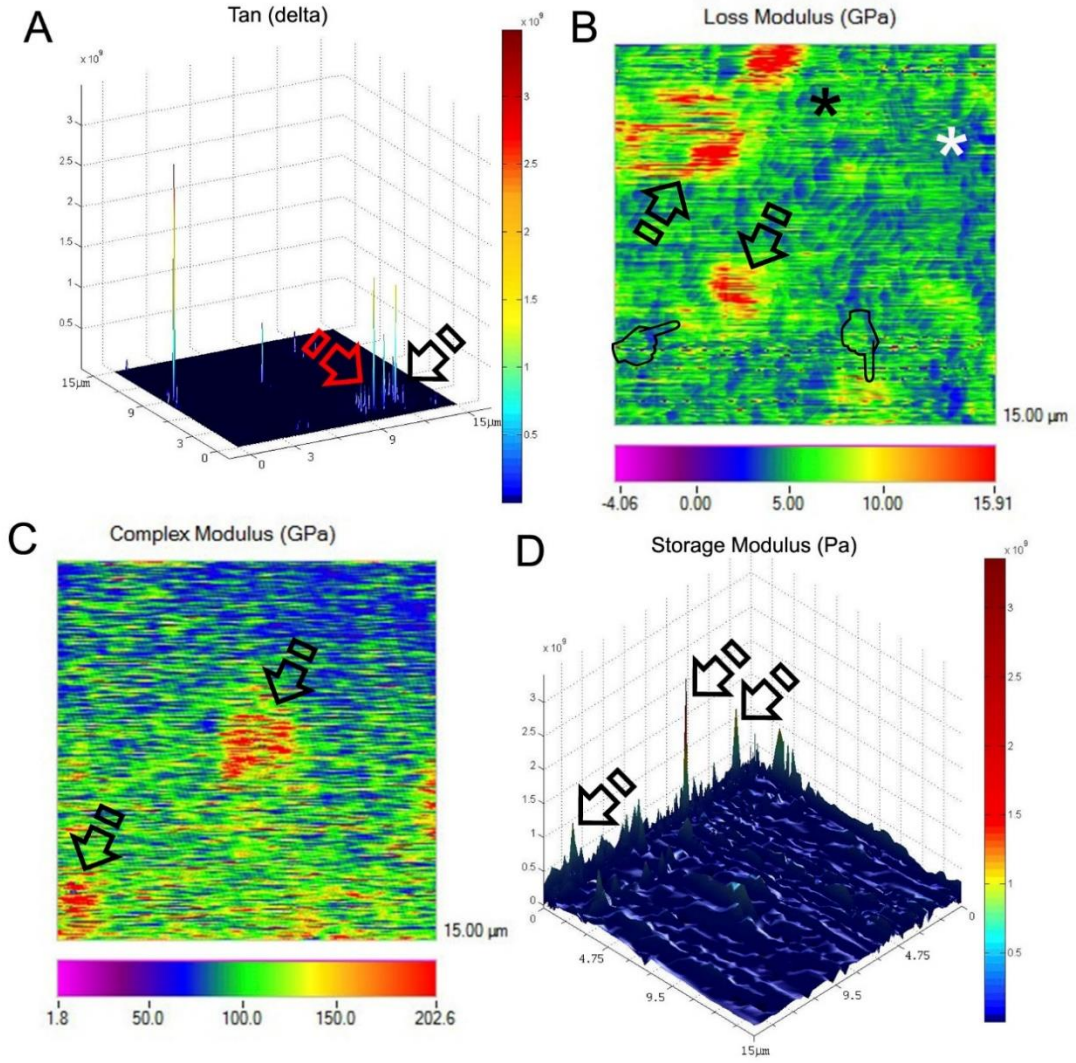

Fig. S2. **A**, 3-D contour map of the tan δ distribution in a specimen at the Dex-NPs/24 h group. In the color scheme shown, the redder color corresponds to higher values of the locally measured moduli. At the resin-NPs-dentin inter-diffusion zone, tan δ obtained the highest values, among groups, at 24 h, creating a zone of lower dissipation of energy, and thereby promoting stress concentration and breaking with failure of the dentin interface (arrows). Magnitudes of X, Y and Z axis are in microns. Magnitudes of X and Y axis are in microns. **B,** Scanning mode nano-DMA analysis of the map of the loss modulus/*E''*, at the Dex-NPs/24 h group. In the color scheme shown, the redder color corresponds to higher values of the locally measured moduli. Wider circles of higher loss modulus, represented in red, are unveiled (arrows), corresponding to the peritubular and intratubular dentin. They are immersed in an extended area of a lower *E''*, represented at the mapping in yellow (pointers), corresponding with the intertubular dentin. The rest of the interface appears in blue and green (asterisks). **C**, Scanning mode of nano-DMA analysis of a map of the complex modulus/*E** distribution in a specimen at the Dex-NPs/21 d group. In the color scheme shown, the redder color corresponds to higher values of the locally measured moduli. At the NPs-dentin inter-diffusion zone, *E** obtained the highest values, among groups, at 21 d, creating a zone of higher resistance to dynamic deformation or robustness (arrows). **D**, 3-D contour map of the storage modulus /(*E'*) distribution in a specimen at undoped-NPs/21 d group. In the color scheme shown, the redder color corresponds to higher values of the locally measured moduli. Peritubular dentin (arrows) showed the highest elastic behavior (*E'*) as shown in the redder-yellow areas Magnitudes of X and Y axis are in microns.

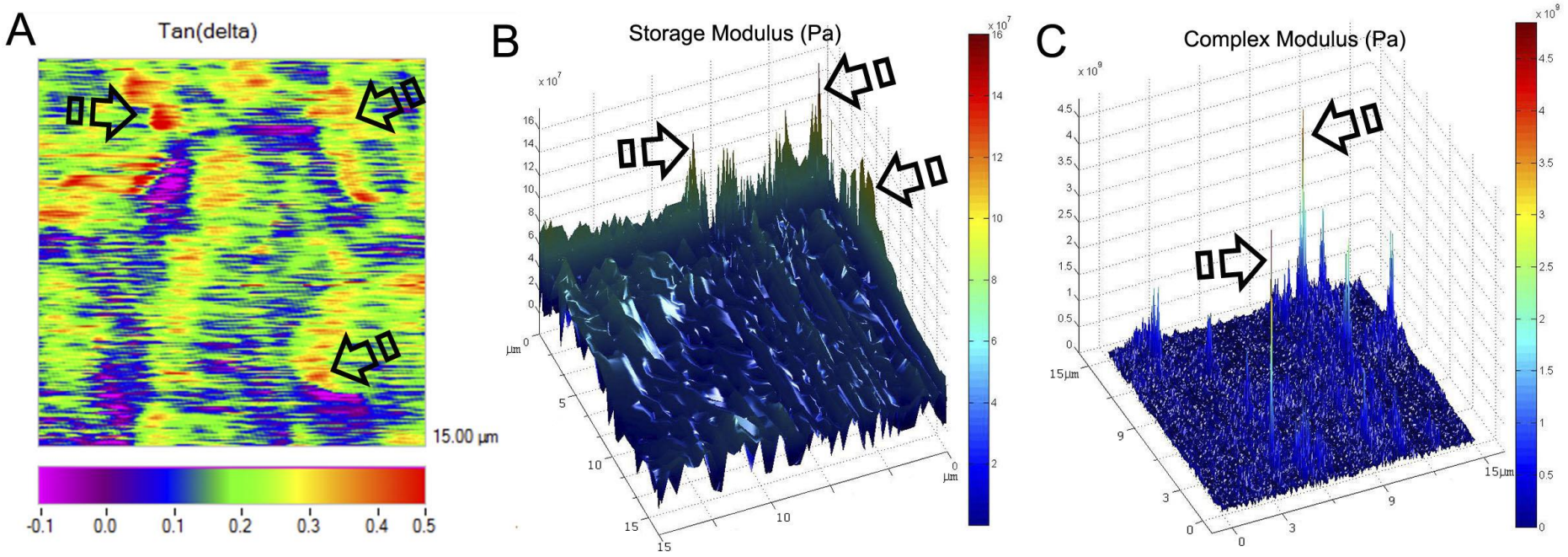

Fig. S3. **A**, Scanning mode of the tan δ distribution in a control specimen/24 h group. In the color scheme shown, the redder color corresponds to higher values of the locally measured moduli, related to tubular structures (arrows). **B**, 3-D contour map of the storage modulus (*E'*) distribution in a sample at the control specimen/21 group. In the color scheme shown, the redder color corresponds to higher values of the locally measured moduli. Peritubular dentin (arrows) showed the highest elastic behavior (*E'*) as shown in the redder areas. **C**, Scanning mode nano-DMA analysis of the map of the complex modulus/*E**, at the Zn-Dex-NPs/21d group. In the color scheme shown, the redder color corresponds to higher values of the locally measured moduli. Red-yellowish peaks point out areas of *E** associated with peritubular and intratubular dentin (arrows), potentially related to mineralization. Magnitudes of X and Y axis of 3-D contour maps are in microns.

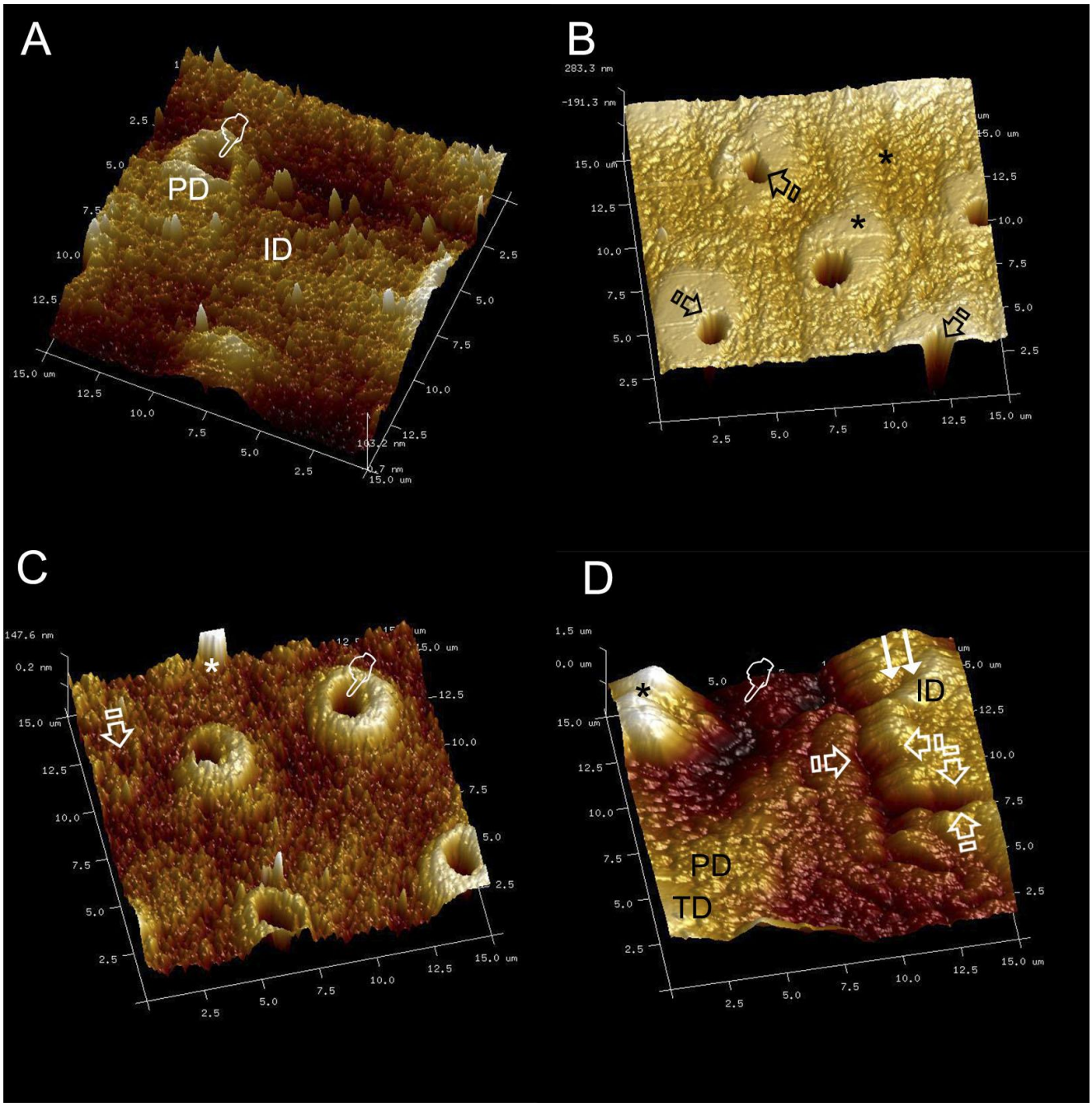

Fig. S4. **A**, AFM 2.5 x 2.5 µm top-view and surface plot image of untreated dentin, at 24 h of storage. Dentinal tubules remained visible and open (pointer). Intertubular (ID) and peritubular (PD) dentin are clearly discernible. A porous intertubular dentin structure may be observed. **B**, AFM 2.5 x 2.5 µm top-view and surface plot image of a dentin surface treated with undoped-NPs, at 24 h of storage. Dentin appears remineralized (asterisks) and peritubular dentin visibly protrudes on the surface of the specimen narrowing the tubular lumen (arrows). **C**, AFM 15 x 15 µm top-view of topography mapping of dentin obtained after applying Dex-NPs and 24 h storage time. Some dentinal tubules appeared empty (pointer), partially mineral filled (arrows) or totally filled (asterisk). **D**, AFM 15 x 15 µm top-view of topography mapping of dentin obtained after applying Zn-Dex-NPs and 24 h time of storage. PD and ID dentin mineralization is evident. Intratubular dentin (TD) is totally occluding the dentinal tubules (asterisk). Stick-slip images and little rod-like minerals (faced arrows), as bridge-like structures indicating sight of energy dissipation at the limits between both PD and ID are present. NPs were scarcely observed, most of them covered by a layer of mineral (pointer). The crack deflection and branching, around the peritubular cuff, may be observed at the dentinal wall of a dentinal tubule (double arrow).

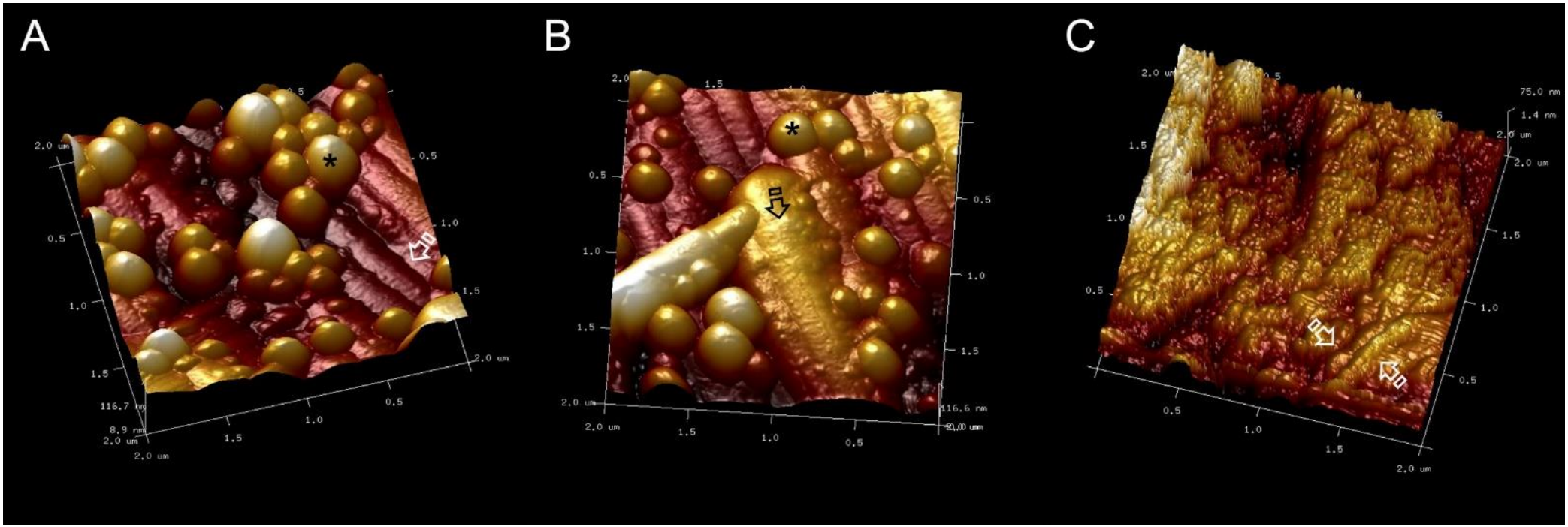

Fig. S5. AFM phase image (2 x 2 μm) when Dex-NPs (**A**) or Zn-Dex-NPs (**B**) were applied on dentin and observed at 24 h time point, showing the wider bandwidth of the collagen fibrils and the staggered pattern of collagen fibrils (arrows). NPs may be intimately adhered to the collagen fibrils (asterisks). **C,** Demineralized collagen fibers were observed in dentin surfaces treated with undoped-NPs analyzed after 21 d time point (arrows).

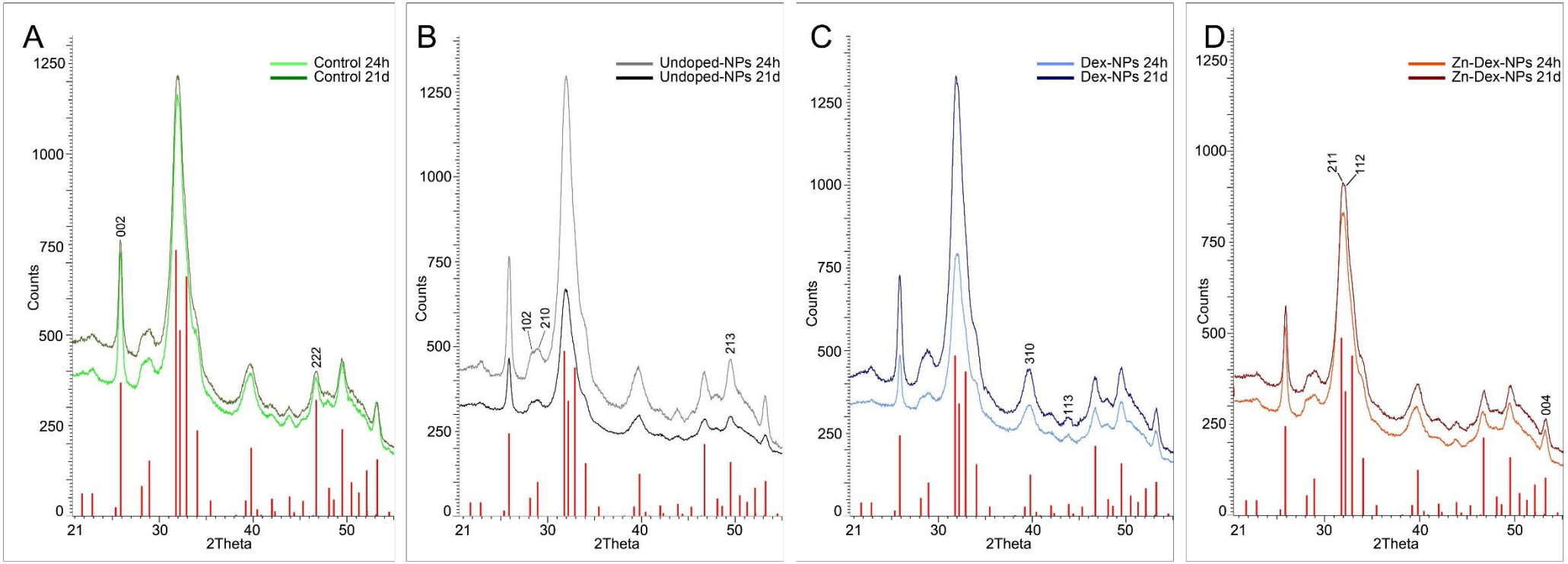

Fig. S6. Insets representing truncated μXRD^2 profiles after observing the reflection from 002 to 004 peaks in the control group (**A**), dentin treated with undoped-NPs (**B**), Dex-NPs (**C**) and Zn-Dex-NPs (**D**), after 24 h and 21 d of PBS storage. Vertical bars represent HAp peaks.

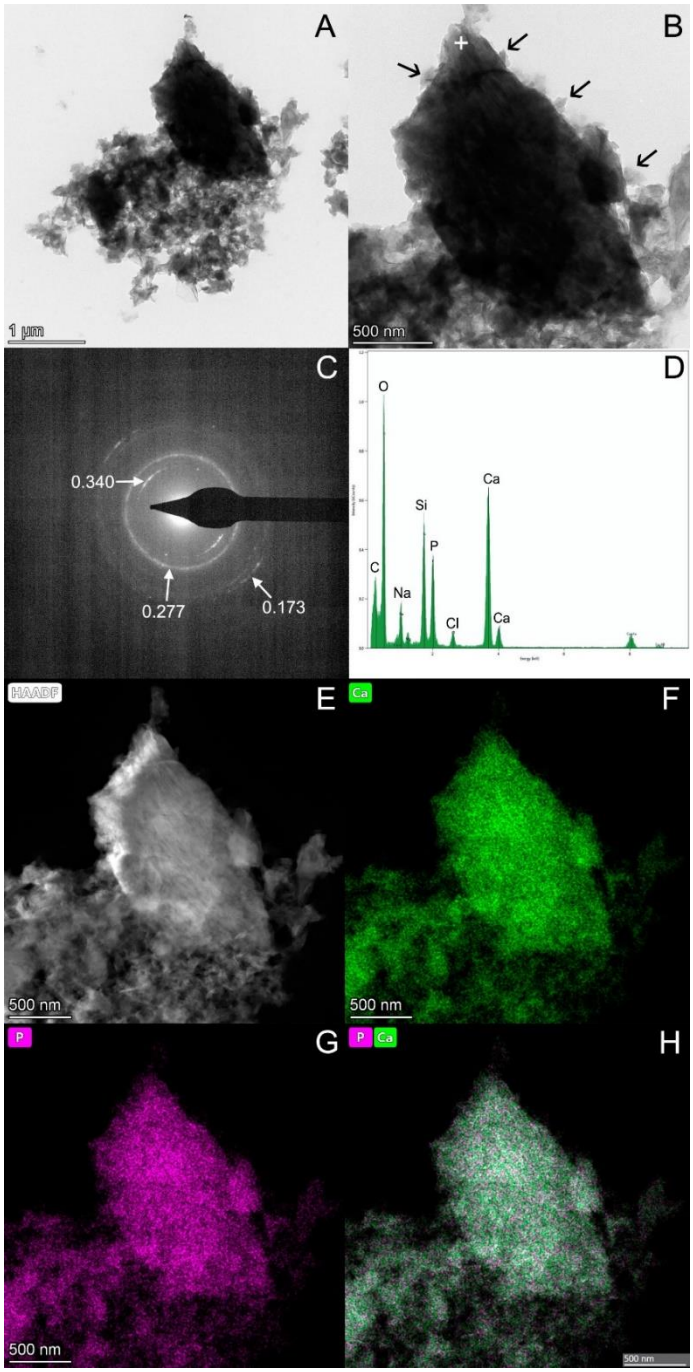

Fig. S7. A, Bright-field of an assemblage of a polygonal block-like apatite of coronal dentin treated with Dex-NPs at 24 h time point. The frame of the pentagonal figure is composed of an assembly of aligned polyhedral sheets of apatite crystals (arrows) (**B**). **C** Shows a specific area electron diffraction (SAED) of the crystals (+) shown in (B), at nanoscale, unveiling a highly polycrystalline structure. Three Debye rings and interplanar distances ranging from 0.34 nm to 0.173 nm were identified. **D,** Representative Energy-dispersive X-ray spectroscopy (EDX) of the crystals (+) observed in (B) showing the nanometer-sized apatite composition of calcium and phosphate as part of the elemental analysis. **E,** Scanning TEM (STEM) bright-field image and EDS-STEM mapping of the crystals (+) observed in (B). **F,** Two dimensional elemental mappings of calcium [Ca], phosphate [P] (**G**), and calcium phosphate [PCa] (**H**).

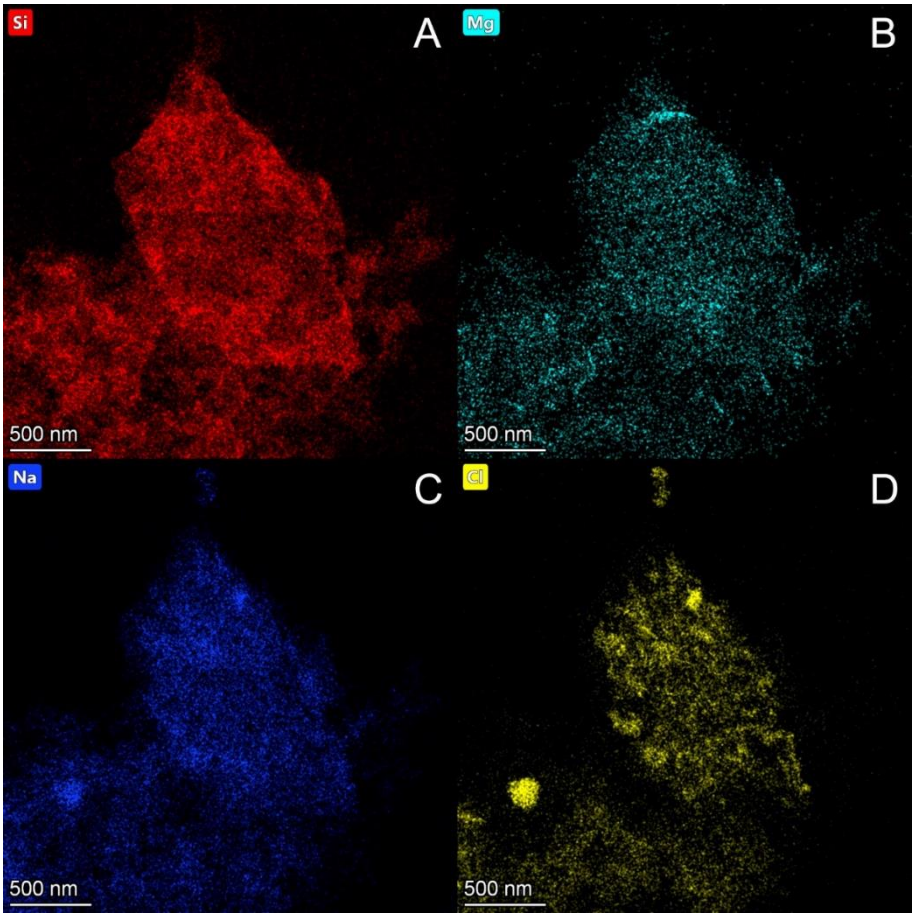

Fig. S8. Scanning TEM (STEM) bright-field image and EDS-STEM mapping of the crystals (+) observed in (Fig. S7) that corresponds to the analysis of coronal dentin treated with Dex-NPs at 21 d time point. **A,** Two dimensional elemental mappings of silica [Si], magnesium [Mg] (**B**), sodium [Na] (**C**) and chloride [Cl] (**D**).

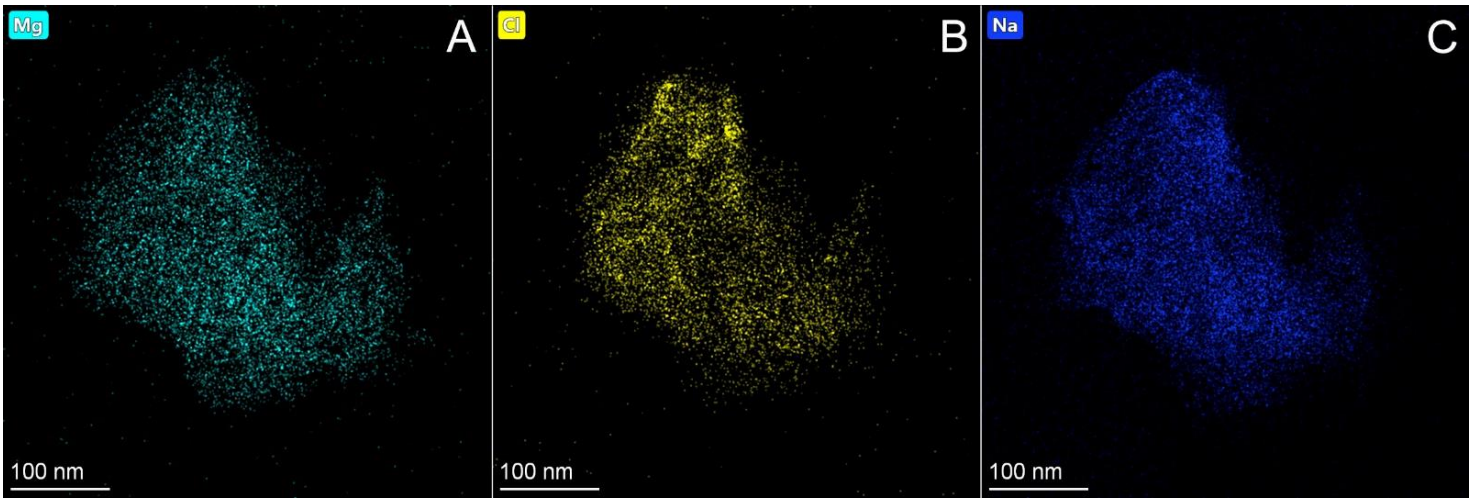

Fig. S9. Scanning TEM (STEM) bright-field image and EDS-STEM mapping of the crystals (+) observed in (Fig. 6) that corresponds to the analysis of coronal dentin treated with Zn-Dex-NPs, at 21 d storage. **A,** Two dimensional elemental mappings of magnesium [Mg], chloride [Cl] (**B**) and sodium [Na] (**C**).

Table S1. Relative intensity (%) of the Hydroxyapatite characteristic diffraction planes obtained in each study group (with a margin of error 1.5%).

Groups	Diffraction planes		
	(002)	(112)	(310)
Control	37	97	17
Undopeds-NPs	40	99	17
Dex-NPs	34	98	16
Zn-Dex-NPs	38	99	18

For all the diffraction patterns, the peaks values had been normalized at maximum to the intensity of the 211 peak basis near 31.90 2Theta.